Micropatterned Heater for Multiplexed Nanoplasmonic Sensing

Master's thesis in Nanotechnology

MARTIN SECH

MASTER'S THESIS 2019

Micropatterned Heater for Multiplexed Nanoplasmonic Sensing

MARTIN SECH

Micropatterned Heater for Multiplexed Nanoplasmonic Sensing
MARTIN SECH

Cover: Isothermal contours in one of the modelled multiplexing sensors, when three of the regions are heated.

Micropatterned Heater for Multiplexed Nanoplasmonic Sensing
MARTIN SECH
Department of Physics
Chalmers University of Technology

Abstract

In order to utilise nanoplasmonic sensing for air quality measurements, the temperature of the sensing layer must be controlled. This is possible through the use of a microheater localised on the sensor, which trough Joule heating can make it possible to manage the sensor's temperature with high accuracy. However, the microheater's design can determine both energy efficiency and the sensing properties of the sensor, hence careful design and characterisation of the micropatterned heater must take place in order to optimise it. Further more, for multiplexed sensing where several air pollutants are measured simultaneously, the microheater must be able to maintain several distinct temperatures on the same sensor.

In this thesis, several sensors with new geometries have been modelled and fabricated, both for the purpose of multiplexing and to yield lower power consumption. By using thermoresistive measurements on the microheaters, it was determined that it was possible to decrease the power consumption up to 51 % by lowering the sensor thickness and decreasing the size of the heated region. Through the use of thermal imaging, it was also confirmed that the temperature uniformity of the heated region could be increased by introducing a laser cut groove or gap around it. For the multiplexing sensors, which were designed to be able to sense at least four different gases, heating one distinct region to 120 °C resulted in the remaining sensing areas to reach temperatures of 30-43 °C.

Acknowledgements

First of all, I would like to thank the whole team at Insplorion for being so welcoming and making this spring such an enjoyable and memorable time. Among them, I especially want to thank my two supervisors, Olof Andersson and David Nilebo, for supporting me with my thesis. I would also like to express my appreciation to Per Klockar for giving me practical help, as well as advice, regarding electronics and measurements.

From the chemical physics division at Chalmers, I would like to thank Joachim Fritzsche for both performing the sensor fabrication as well as discussing it with me and sharing his insights. I am also grateful to David Albinsson for allowing me to borrow and do measurements with the IR-camera.

Finally, I want to thank my family and friends for supporting me both during and before my thesis.

Martin Sech, Gothenburg, June 2019

Contents

List of Figures

List of Figures

List of Tables

List of Tables

Abbreviations

HCL	Hole-colloidal lithography
HMDS	Hexamethyldisilazane
IPA	Isopropyl alcohol
LED	Light emitting diode
LSP	Localised surface plasmon
LSPR	Localised surface plasmon resonance
MEMS	Microelectromechanical systems
NPS	Nanoplasmonic sensing
PCB	Printed circuit board
PDDA	Poly(diallyldimethylammonium) chloride
PMMA	Poly(methyl methacrylate)
PS	Polystyrene
RTD	Resistance temperature detector
SMO	Semiconducting metal oxide
TCR	Temperature coefficient of resistance
WHO	World Health Organisation

Abbreviations

1

Introduction

Today, air pollution is a great environmental challenge in many areas around the globe, affecting countries with both low and high economic income levels [1]. Approximately, 91 % of the world's population lives in areas with air containing pollutant concentrations exceeding the safety levels set by the *World Health Organisation* (WHO). This leads to health problems such as lung cancer, respiratory diseases, heart disease and stroke.

In order to start improving air quality, a reliable and efficient tool is needed to monitor pollutants like e.g. nitrogen oxides (NOx), sulphur dioxide (SO_2), carbon monoxide (CO) and ozone (O_3). A possible solution to this is the relatively new optical technique of *nanoplasmonic sensing* (NPS) which is based on the theory of *localised surface plasmon resonance* (LSPR) [2]. Briefly described, LSPR refers to the the fact that conductive nanoparticles will absorb light of one or more frequencies much stronger compared to other frequencies of light. These resonance frequencies are very dependent on the refractive index of the surroundings, which allows highly sensitive measurements of the surface chemistry on the nanoparticles. This makes NPS a very promising technique for air quality sensors, as it can readily detect the adsorption or interaction of gas molecules with the nanoparticles, or a material adjacent to the nanoparticles. However, the effectiveness (kinetics and specificity) of this interaction, as well as the refractive index of the surroundings, are also temperature dependent. This establishes a need for some method applicable to nanoplasmonic sensors, which can be used to control the temperature of the sensor.

Furthermore, an important aspect of NPS sensors for gas sensing is the possibility of multiplexing, i.e. using the sensor to measure several different variables. In the case regarding air quality measurement, multiplexing then refers to measuring the concentration of several different hazardous substances common in polluted air, simultaneously. In multiplexing applications, the possibility of maintaining different temperatures on different parts of the sensor is important, as that allows conditions which are optimal for measuring each substance.

Insplorion, a company working with NPS-technology, currently has a functioning air quality sensor prototype, *InAir*, which is able to determine the ambient NO_2-concentration. In order to reach the right temperature for sensing, an electrical power is applied to a so called microheater, an electrically conducting micropattern, which is localised on the sensor. When the current goes through the microheater, heat will be developed as a result of the electrical resistance and the temperature

will rise. By controlling the applied power to the device, it is then possible to control the temperature. However, in order for the sensor to be suitable for commercial use, it is important that this process is energetically efficient.

1.1 Aim and project outline

The aim of this project is to develop or create the groundwork for an energy efficient microheater which enables multiplexed nanoplasmonic sensing for Insplorion's current version of *InAir*. This will be done by first modelling the currently used microheater and introduce geometric alterations to this model, which are believed to yield better sensor properties. Depending on this investigation, several new sensor designs will be fabricated, characterised and compared to the current sensor. The remaining part of the project will then focus on developing a sensor design which supports multiplexing, which means that the sensor must be able to maintain distinct temperatures on different parts of the sensor. This will also be done by first investigating some designs through modelling, before deciding which to fabricate and characterise. The previous results from the fabricated non-multiplexing sensors will be applied when designing these multiplexing sensors, in order to achieve high energy efficiency.

2

Theoretical background

2.1 Nanoplasmonic sensing

When a metal is exposed to an electromagnetic wave, the free electrons within the material will collectively oscillate, resulting in the formation of plasmons which are the quanta of the oscillation [3]. At the interface between a metal and a dielectric material, surface plasmons will occur, which formally are referred to as surface plasmon polaritons.

In nanoplasmonic sensing, so called *localised surface plasmons* (LSPs) are utilised [2]. These are surface plasmons contained in nanoparticles where the confinement size of the plasmon is relative to the wavelength of light, which leads to several interesting effects. The distinct property of LSPs is that electric fields near the surface of the nanoparticle are greatly enhanced, but decays quickly away from it, making the enhancement highly localised. Another important trait of LSPs is that the light extinction (sum of absorption and scattering) is strongest at the resonance frequency of the LSP [3]. Using Mie theory, i.e. the theory of how spherical particles scatter and absorb light, the optical extinction cross-section σ_{ext} can be approximated as

$$\sigma_{ext} = \frac{18\pi\varepsilon_m^{3/2}V}{\lambda}\frac{\varepsilon_2(\lambda)}{\left(\varepsilon_1(\lambda) + 2\varepsilon_m\right)^2 + \varepsilon_2(\lambda)^2} \tag{2.1}$$

where ε_m is the dielectric function of the surrounding medium, V is the volume of the particle, λ is the wavelength of light, ε_1 and ε_2 are the real and imaginary parts of the dielectric function of the metal, respectively. Note from equation 2.1 that σ_{ext} is maximised when $\varepsilon_1 = 2\varepsilon_m$, which gives the condition for the LSPR. This condition also reveals how very dependent the LSPR-frequency is on the surrounding of the nanoparticles, i.e on ε_m, which is the basic principle behind its usefulness in sensing applications. Though, the properties of the nanoparticles themselves also affect it strongly, e.g. particle material, size and shape. By combining this resonance condition together with the classical Drude model, which describes electrical conduction in metals, it is possible to get an explicit expression for the LSPR-wavelength λ_{max},

$$\lambda_{max} = \lambda_p\sqrt{2n_m^2 + 1}, \tag{2.2}$$

where λ_p is the plasma wavelength of the metal, and n_m is the refractive index of the surrounding medium (related to the dielectric function of the medium as $\varepsilon_m = n_m^2$). As seen from equation 2.1, the wavelength peak position is approximately proportional to n_m.

Note that even though Mie theory is based on spherical nanoparticles, LSPs can also occur for other shapes. Gans theory expands the results from Mie theory to also include spheroid nanoparticles of arbitrary aspect ratio. The main consequence is that the number of plasmon peaks will be equal to the unique dimensions of the particle, i.e. a nanosphere will have one plasmon peak, while a prolate nanospheroid will have two plasmon peaks. However, for more complicated shapes, Gans theory might not hold true. A common particle shape and setup used for NPS is to design the sensing area as an array of nanodiscs, fabricated using e.g. *hole-mask colloidal lithography* (HCL) [4], as this often leads to high refractive index sensitivity [5].

NPS can be either direct or indirect [5]. In the first case, the nanoparticles themselves undergo a change which results in a shift in λ_{max}, while in the second case, it is a change in a material adjacent to the nanoparticles which is responsible for the peak shift. Such a shift of λ_{max} in the optical extinction can be seen in figure 2.1. Note that, though the peak shift is the most commonly used parameter for sensing, there can also be a change in the amplitude of the peak and full width half maximum $fwhm$, which also could have use in analysis.

In indirect NPS, which is utilised in *InAir*, temperature is an important parameter that can affect the peak position [6]. Although this makes it possible to use NPS for making nano-thermometers, it can also make it complicated to analyse signals in which the peak position is simultaneously affected by both a change in concentration and temperature.
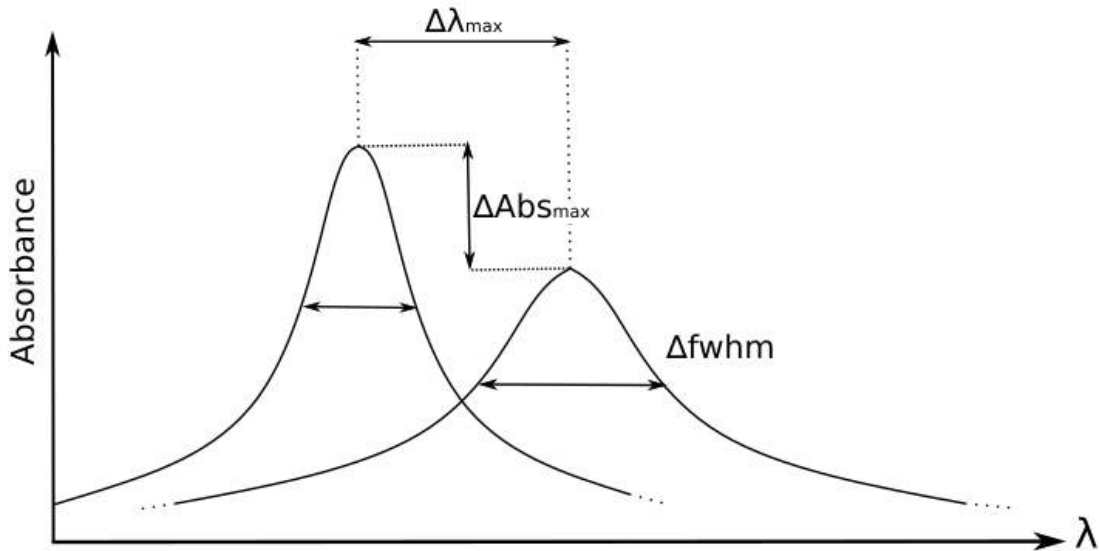
Figure 2.1: A schematic of how the plasmon peak changes due to some process. The shift in peak position, $\Delta\lambda_{max}$, is mainly used in sensing applications, but the change in peak amplitude, ΔAbs_{max}, and full width half maximum, $\Delta fwhm$, can also be useful.

2.2 Semiconducting metal oxides and gas kinetics

An alternative to the NPS gas sensor is one that is based on the resistivity properties of *semiconducting metal oxides* (SMO) [7]. At temperatures of 200-400 °C, these materials have a drastic change in electrical conductivity when exposed to certain gases, which can be utilised for sensing. However, they have also been showing promise for increasing selectivity in high-temperature NPS gas sensing when used as an adjacent material to the nanoparticles [8, 9]. By choosing the right SMO material, composition, morphology and temperature, it is possible to get a sensor that is highly selective to only one or a few gases. The mechanism that causes this high selectivity is still relatively unclear, but it is believed to be due to charge exchange between the SMO and the nanoparticles [8]. When gases interact with the SMO, they can either oxidise or reduce it, which typically will result in red-shifting or blue-shifting of the plasmon peak, respectively. Additionally, this process can also affect the dielectric constant near the nanoparticles, which in turn will affect the plasmon peak as discussed previously.

As mentioned, the temperature is a very important parameter for the selectivity, which is due to its strong effects on the kinetics of the process [10]. For a certain temperature and gas, there will be a certain surface concentration due to the specific rate of adsorption and desorption of the gas molecules. When the SMO is exposed to several gases, as is the case in air, the different gas molecules will compete for adsorption sites. In regular ambient environment, the SMO surface is covered in majority by oxygen ions. For oxidising gases, these oxygen ions are simply replaced by said gas. For reducing gases, this adsorption process is more complicated, as these will react with adsorbed oxygen ions to form some redox product, e.g. water molecules, which needs to escape the surface before more gas can be adsorbed. Regardless of the exact mechanism, it is possible to maximise the selectivity for a certain gas by choosing the optimal temperature. However, the quality of this selectivity is still limited by previously mentioned factors, such as the properties of the utilised SMO.

2.3 Overview of microheaters

A microheater, or micro-hotplate, is an electrically conducting thin film on top of a substrate, that is heated through so called Joule heating, i.e. the heat production that follows when an electric current flows through a material [11, 12]. Due to their good high-temperature control and relatively small power consumption, microheaters have applications in several *microelectromechanical systems* (MEMS), where the largest area of use is within MEMS gas sensors, such as e.g. SMO gas sensors [11].

There are four main types of microheaters, as seen in figure 2.2a. The microheater can either be located directly on top of the substrate, on a closed or open membrane, or on a cantilever. To achieve minimal power consumption, the three latter types are preferred, as that ensures minimal thermal conduction to the surroundings of the

microheater. However, the disadvantage of those types is that they have a lower mechanical stability compared to simply having the microheater on a substrate. This is especially a problem at higher temperatures where thermal expansion of the thin film and membrane is more considerable. Electromigration, the gradual movement of conductor ions in the metal due to high current density, will also be more prominent for higher temperatures and might cause the wire to break. Subsequently, the lifetime of a microheater is always lower when it has a higher work temperature.

The materials used in the microheater are also very important. Typically the conducting layer is made of metal, ceramic or doped polysilicon, where the first mentioned is the most commonly used. Ideally, the conductor should have low mechanical sensitivity to temperature, be inert and have low electrical resistance. The reason for why the latter is desired is explained by Ohm's law,

$$U = RI = \sqrt{RP} \tag{2.3}$$

where U is the voltage, R is the resistance, I is the current and P is the electrical power. A lower resistance yields a lower voltage for a certain power consumption, which is a criteria for having the microheater driven by a light-weight battery.

Depending on the thickness of the conductive layer, the material properties might differ from that of the bulk material, as explained in section 2.6. For the material of the substrate or membrane below the microheater, it is generally desired for it to have low thermal conductivity in order to decrease the power consumption of the device.

Another very important aspect of the microheater is the geometry of the conductive micropattern. Two examples of such geometries, the double spiral and meander designs, are shown in figure 2.2b. In MEMS gas sensing applications, the microheater should ideally result in a uniform temperature profile, as the sensing area otherwise probes the environment differently depending on the spatial position. Hence, the microheater geometry should be designed to satisfy this criteria, which the double spiral geometry seems to be the most suitable for [12]. Alternatively, a thin layer of material with high thermal conductivity can be implemented underneath or above the microheater structure. Both geometries shown in figure 2.2b are rectangular, but there are several advantages with utilising a circular geometry instead. For example, a circular shape leads to more area efficient shape and hence a lower power consumption. Additionally, since a circular microheater lacks corners, it also lacks spots which are sensitive to localised mechanical deformation. However, mask designing for lithography is often more complex for circular shapes compared to rectangular ones.

Note from figure 2.2b that four probes are used on the microheater. Two of these are used to supply the electrical power while two are used to measure the electrical resistance, which often is useful to know for temperature measurement and control, see section 2.5. The benefit of doing a four-probe measurement, compared to a two-probe measurement, is that the contact resistance is accounted for in the former

2. Theoretical background

method, which yields a smaller measurement error and hence is especially important when measuring smaller resistances.

The so called thermal response time, i.e. the time it takes for the microheater to reach a constant temperature, is generally desired to be low in order get a quickly responding heater [13]. The thermal response time t can be found from the expression

$$T(t) = T_{amb} + PR_{therm}\left(1 - e^{-t/\tau}\right) \tag{2.4}$$

where T is the temperature of the microheater, T_{amb} is the ambient temperature (assumed to be the minimum temperature), R_{therm} is the total thermal resistance of the heater and $\tau = R_{therm}C$ is the thermal time constant, where C is the overall heat capacity. The simplest way of decreasing thermal response time is to decrease the overall heat capacity of the heater by lowering its mass, e.g. through scaling it down. Another benefit of having a low thermal response time is that it allows for the microheater to be operated in heat-pulse mode, where the electrical power is applied in pulses rather than in a continuous manner [14]. This can result in a lower power consumption and longer lifetime of the device.

(a)   **(b)**
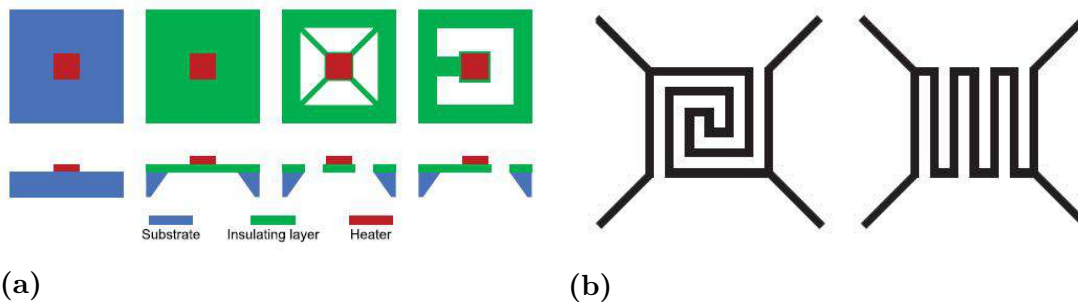
Figure 2.2: (a): Four different microheater types, from left to right; microheater on substrate, open membrane, closed membrane and on cantilever. Blue indicates substrate, green indicates an insulating layer (the membrane material) and red indicates the microheater. **(b)**: Two different types of common microheater geometries; double spiral (left) and meander (right). In both geometries, four probes can be seen, where typically two are used to supply the electrical power and the remaining pair is used to measure the electrical resistance in the heater. Both images are from [11], ©2017 IEEE.

2.4   Heat transfer mechanisms

Fundamentally, there are three heat transfer mechanisms; conduction, convection and radiation [15]. The first mentioned mechanism, conduction, occurs due to interactions between molecules, where the higher energy molecule will lose some of its kinetic energy to adjacent molecules with lower energy, which will lead to a lowering of the temperature gradient in the system. In metals or other materials with high electrical conductivity, heat conduction can also occur through electron transport,

which explains why metals tend to be good heat conductors. The overall three dimensional heat conduction rate $\mathbf{q}_{cond}$ is given by

$$\frac{\mathbf{q}_{cond}}{A} = -k\nabla T \tag{2.5}$$

where A is the area normal to the heat flow, k is the heat conductivity, ∇T is the temperature gradient. For microheaters, conduction occur through the substrate and/or membrane, as well as through the electric contacts and to the surrounding air, and is often the most important heat loss mechanism [11].

Convection involves the heat transfer between a surface and an adjacent fluid (a liquid or gas) [15]. When the fluid flows past the surface with a certain velocity, the convection is referred to as forced, and when the fluid initially is stationary it is referred to as natural or free. Note that in the latter case with free convection, the fluid will still move due to circulation. As the fluid near the hot surface gets warmer, its density will decrease and it will rise, where it eventually will cool of and circulate back down, and so on. The one-dimensional convective heat transfer q_{conv} is given by the Newton rate equation,

$$\frac{q_{conv}}{A} = h\Delta T \tag{2.6}$$

where h is the convective heat transfer coefficient and ΔT is the temperature difference between the surface and fluid. h is a function of the system geometry, fluid and flow properties, and ΔT, which often can be found by utilising certain correlations. Comparing forced and free convection, h is usually greater for the former as it typically involves a higher rate of mass exchange. For microheaters, it is not entirely established if convection plays a major part or not in the heat loss [11]. Due to the restricted air flow in small sensors, convection might be neglected in some cases [12]. On the other hand, mixed convection, i.e. when both free and forced convection occur simultaneously in a coupled manner, has also been shown to be relevant for some microsystems [16]. Nonetheless, if the microheater is used in a vacuum environment, which is the case in certain applications, there will be no heat transfer by convection as there is no surrounding fluid [12].

The last mechanism of heat transfer is radiation, where the the energy is transferred by photons being emitted from a surface [15]. The one-dimensional radiant heat transfer q_{rad} from a surface is given by

$$\frac{q_{rad}}{A} = \frac{\sigma}{\varepsilon} T^4 \tag{2.7}$$

where $\sigma = 5.676 \cdot 10^{-8} \, WK^4/m^2$ is the Stefan Boltzmann constant and ε is the surface emissivity, which is a number between 0 and 1 that indicates how efficient the surface is at sending out radiation. $\varepsilon = 1$ indicates a black-body, which is the ideal radiating surface. Note that in reality, ε depends both on wavelength, direction and in some cases also on the temperature of the surface. For microheaters, radiation losses are often small, but due to the strong temperature dependence in equation 2.4, it can be very relevant for temperatures above 500 °C [11].

2.5   Temperature characterisation of microheaters

In order to control the temperature in a microheater through e.g. a feedback mechanism, some method must be used to establish the temperature. A common method, which currently is utilised in *InAir*, is through a *resistance temperature detector* (RTD) [17]. In these thermoresistive sensors, the intrinsic temperature dependence of the electrical resistance is utilised to measure the temperature of a conductor, whose electrical resistance is given by

$$R(T) = \frac{\rho(T)L}{wt} \qquad (2.8)$$

where ρ is the electrical resistance, L is the length or the conductor, w is the width of the conductor and t is the thickness of the conductor [18]. The temperature dependence of ρ is often assumed to be linear, such that

$$\rho(T) = \rho_0 \left(1 + \alpha(T - T_0)\right) \qquad (2.9)$$

where ρ_0 is the electrical resistivity at the reference temperature T_0 and α is the *temperature coefficient of resistance* (TCR). For the RTD, the material should be chosen such that the temperature dependence is maximal, i.e. α should be large. It is usually not a problem that α is not known exactly beforehand, since it can be found through calibration. However, α can change over time due to material degradation and might also be sensitive to hysteresis effects.

Furthermore, as for microheaters, thermal expansion due to high temperatures might also be a problem [18]. If the conductor thermally expands, its dimensions changes and as seen from equation 2.8 this will change the resistance, which incorrectly might be interpreted as a change in temperature. Another regular problem for RTDs is self-heating, i.e. the current used in the RTD for the resistance measurement will increase its temperature which in turn will lead to a measurement error. For a microheater, the heating wire in the microheater itself can be utilised as an RTD [17]. Alternatively, one can fabricate a separate RTD on the microchip, but then there will be a temperature drop due to the distance between the microheater and the RTD.

An alternative non-contact method to investigate the temperature on a microheater is by using an IR-camera to perform thermal imaging [17]. Even though this characterisation method has no risk of affecting the microheater, the measurement errors are often more considerable. For example, thermal imaging is very dependent on the emissivity of the material which must then be known to correctly convert the measured radiation units into temperature units. Neither is the calibration straightforward, due to several factors. For one, the relationship between photon flux and detector response cannot be assumed to be linear, so two calibration points will not suffice [19]. Secondly, the response of the camera pixels across the detector is non-uniform, which requires individual correction factors for the different pixels. Lastly, there is a temperature drift of the detector and other compartments of the camera

during use, which might cause the response to vary with time [20]. Regardless, thermal imaging remains a popular approach to visually characterise the temperature distribution on microheaters [17].

2.6   Thin film effects

Due to the micro- or nano sized thickness of thin films, they often have different properties compared to their bulk counterpart. For microheaters, one of the most important properties that is affected is the conductor resistivity [11]. For metal thin films with thicknesses below 200 nm, the resistivity will be considerably higher than the corresponding bulk metal. This can be explained by Matthiesen's rule,

$$\rho = \rho_l + \rho_i \tag{2.10}$$

 in which the metal resistivity is assumed to have two different sources [21]. ρ_l is the resistivity caused by the lattice, or rather electrons interacting with phonons in the material, i.e the quanta of lattice vibration. ρ_i is the collective resistivity caused by static defects such as impurities, grain boundaries and film boundaries. Since a thin film will have a larger relative surface area, the latter term and hence the resistivity of the material will be larger [22]. Furthermore, ρ_i is approximately independent of temperature, while ρ_l has a strong temperature dependence. Since the ρ_i-term is more dominant for thin films, this means that the thin film resistivity is less temperature dependent compared to the bulk counterpart. In other words, for a lower film thickness, the TCR will decrease.

For thin films, the thermal properties might also differ from that of bulk materials [11]. The heat conductivity is often smaller for metal thin films due to increased phonon scattering on the film surface, analogously to how the electrical resistivity increased due to increased electron scattering. The surface emissivity will also be considerably larger for metal thin films with 100 nm thickness or lower, due to increased internal reflection.

It should be noted that thin film properties are not only dependent on the film thickness, but also rely heavily on the fabrication procedure. This is because different microfabrication methods will lead to thin films with e.g. different grain size, grain shape, purity and residual stress. Furthermore, thin film properties can be adjusted after fabrication by certain methods, e.g. by thermal annealing above the recrystallisation temperature [22]. This will induce grain growth in the metal thin film and hence reduce the number of grain boundaries in the material, which consequently will lead to lower resistivity and higher TCR as discussed above.

2.7   The air quality sensor

Insplorion's current device for air quality sensing, *InAir*, can be seen in figure 2.3. Currently, the sensor can measure NO_2-content in air down to the ppb-level. The 5 mm diameter inlet, seen in the image, allows air to pass through the device with

a flow velocity of 300 ml/min or lower. The majority of the device is occupied with electronics, but the component that allows for NPS is a 5 x 5 x 1 mm sensor, whose layer structure is schematically shown in figure 2.4. The sensor utilises an array of gold nanodiscs which is covered by a sensing layer that increases the NO_2 selectivity. It is this side of the sensor that is illuminated by a white *light emitting diode* (LED), whose light will interact with the gold nanodiscs and eventually reach a detector where it can be used for NPS-analysis.

In figure 2.5a, the current platinum (Pt) microheater pattern can be seen, whose geometry can be identified as a circular double spiral. A couple of electrodes are in contact with the metal layer at the south edge on each side of the air gap, as shown in figure 2.5b, which will cause an electric current to flow between them trough the spiral geometry. Due to the much smaller dimensions of the spiral wire, Joule heating only occurs in that part of the layer. Since the substrate is covered by metal outside the spiral area, these electrodes can be applied easily even without high precision. Additionally, this pattern will ensure that light will only go through the spiral area (the light going through the non-covered strip below the spiral can be neglected). Only the sensing area approximately parallel to the double spiral will be sufficiently heated to be utilised for NO_2-sensing, hence this is desired as it blocks all light from the non-active area that would otherwise perturb the signal. For this report, the work temperature of the device has been assumed to be 120 °C to sense NO_2.

Figure 2.3: Current prototype for the *InAir*-device. The inlet, shown in the image, allows air to flow through the device to the outlet, which is localised on the opposite side of the inlet.
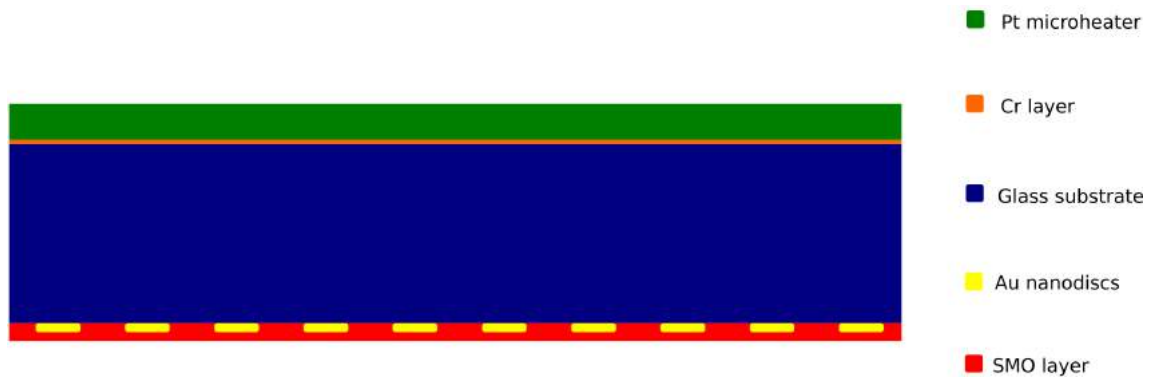
Figure 2.4: A schematic cross-section view of the 5 x 5 x 1 mm sensor. The green layer is the microheater layer, which is approximately 200 nm thick and is made of platinum. The blue layer is the 1 mm thick glass (fused silica) substrate. In between the platinum and the substrate, there is a 10 nm chromium (Cr) layer, shown in orange, which has the function to increase the microheater-substrate adhesion. Attached to the substrate layer, there is an evenly distributed array of gold nanodiscs with diameters of 100 nm and heights of 20 nm. Subsequently, there is a layer shown in red which is the SMO layer, that is several tens of nm thick. Note that the different layers in the figure are not correctly scaled in comparison to each other.

(a) **(b)**
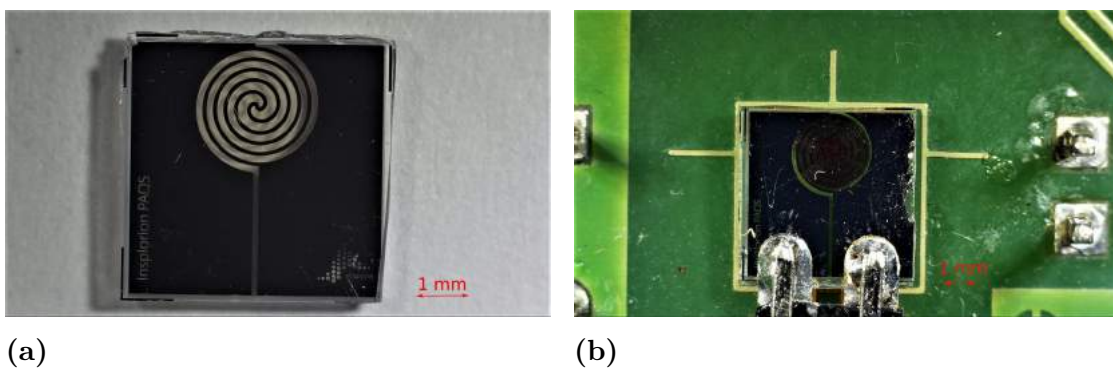
Figure 2.5: (a): The sensor utilised in *InAir*, with the metal layer facing upwards. **(b)**: The sensor when attached in the device by the electrodes, shown in the bottom of the image. The detector is below the spiral area, while the LED lamp (which is not attached in the image) would be above the sensor.

3
Methods

3.1 Development of model for microheater

Before fabrication and characterisation, COMSOL Multiphysics was used to model the current microheater, whose geometry can be seen in figure 3.1. In the model, an electrical power is applied to the the south edge of the platinum layer, left to the air gap. The electrical current then goes through the spiral to the other south edge of the platinum layer, which is grounded. Due to Joule heating, the temperature will rise in the sensor as the heat is accumulated. Eventually a stationary state will be reached where the applied power will be fully dissipated to the surroundings through conduction, convection and radiation. It is this stationary state that is of prime interest, or more precisely, its temperature profile and required energy consumption.

Thereafter, several alterations were done to the geometry in order to investigate how such alterations might affect power consumption and temperature distribution of the real sensor:
- Reduction of substrate thickness.
- Scale down of the whole sensor chip.
- Alteration of the spiral geometry which will lead to different length and/or thickness of the conducting wire in the spiral.
- Centralisation of the spiral area.
- Alteration of the spiral size.
- Introduction of grooves in the sensor chip geometry.
- More complex alteration of the sensor chip geometry, e.g. forming it in specific shapes.

These modelling results were, together with practical considerations, the motivation for proceeding with fabricating the sensors discussed in section 4.1.3. Different design alternatives suitable for multiplexing were also investigated, for which the primary objective was to design micropatterns that have low heat spread between the active regions. In table 3.1, the different material parameters of interest are shown for the solids used in the model, while the used parameters for air can be seen in table 3.2.

In order to make the model easier to construct and work with, several approximations have been made (listed in no specific order):
- The sensor was assumed to be suspended in an infinite volume of pure air.

Consequently, any heat conduction to the contact electrodes was neglected.

- Due to the thin size of the platinum layer, it was assumed to have no temperature gradient in the direction perpendicular to the layer.
- The electrical resistivity of the platinum layer was assumed to be the same as that of bulk platinum. As an electrical power is used as an input variable (and not a voltage or current), the total resistance of the microheater will have no effect on the resulting temperature profile.
- The air flow into the device is $300\,\text{ml/min}$. Since the cross-sectional area of the device is $7.35\,\text{cm}^2$, this should result in a flow velocity of $0.0068\,\text{m/s}$ reaching the sensor. Due to this low velocity, both natural and forced convection is added to the model. However, since the inlet diameter is approximately $5\,\text{mm}$, the initial velocity is $0.255\,\text{m/s}$ and hence the flow velocity that reaches the the substrate is somewhere between $0.0068\text{-}0.255\,\text{m/s}$. For simplicity's sake the velocity is set to $0.0068\,\text{m/s}$ regardless.
- The heating effect from the lamp sending light through the sensor was neglected.
- The backside of the substrate was assumed to only be glass, even though it in reality is covered by a thin sensing layer. Additionally, the chromium layer between the substrate and platinum layer was neglected.
- When comparing power consumption throughout this report, the applied power is set such that the maximum temperature of the sensor is $120\,^\circ\text{C}$. In reality, $120\,^\circ\text{C}$ is the average temperature of the spiral area, which likely is a few degrees below the maximum temperature.
- The ambient temperature was set to $20\,^\circ\text{C}$, and the ambient pressure to $1\,\text{atm}$.
- No mechanical effects, such as e.g. film expansion, were accounted for.
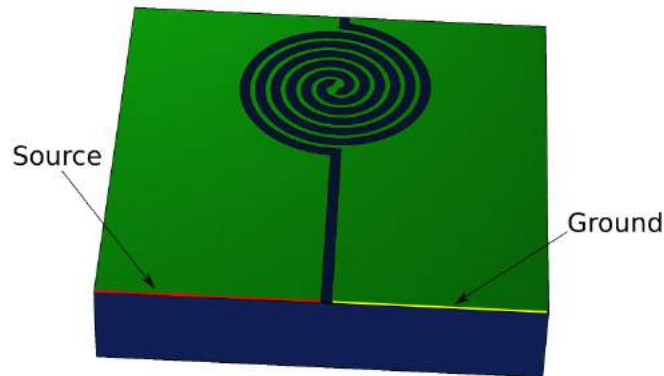
Figure 3.1: The current microheater. The blue block represents the 5x5x1 mm glass substrate, while the green layer on top is the 200 nm platinum thin film. The spiral diameter is set to 2.43 mm, the width of the air gap forming the spiral is 110 µm, the approximate width and length of the platinum wire is 72 µm and 21 mm, respectively. The electrical power is applied to the left south corner (highlighted in red), while the microheater is grounded in the right south corner (highlighted in yellow).

Table 3.1: Material properties for the solids used in the models. If no source is given, the standard value from COMSOL Multiphysics was used. Note that a linear approximation has been assumed for the platinum resistivity, where the temperature unit is K.

Material property	Platinum	Silica glass
Heat capacity $[J/(kg \cdot K)]$	133	703
Density $[kg/m^3]$	21 450	2203
Heat conductivity $[W/(m \cdot K)]$	71.6	1.38
Electrical resistivty $[\Omega \cdot m]$	$1.06 \cdot 10^{-7} \left(1 + 0.00392(T - 300)\right)$ [23]	10^{14}
Surface emissivity	0.104 [15]	0.94 [15]

Table 3.2: Material properties for air at $20\,^\circ$C and $120\,^\circ$C, from COMSOL Multiphysics.

Material property	$20\,^\circ$C air	$120\,^\circ$C air
Heat capacity $[J/(kg \cdot K)]$	1005	1013
Density $[kg/m^3]$	1.204	0.8980
Heat conductivity $[W/(m \cdot K)]$	0.0258	0.0332
Dynamic viscosity $[m^2/s]$	$1.814 \cdot 10^{-5}$	$2.269 \cdot 410^{-5}$

3.2   Sensor fabrication

As described in sections 3.2.1-3.2.2, the sensor fabrication includes both fabrication of the microheater layer as well as fabrication of the sensing gold nanodisc array. These steps were performed on a wafer which subsequently was diced into different sensors. Two of the sensors were also cut by a laser, using a laser machine from the *Epilog Zing Laser* series. Note that, while the sensors typically contain a layer of some thin SMO on the gold nanodiscs as shown in figure 2.4, the sensors tested for this project did not. However, this was assumed to not affect the sensor properties characterised for this project.

3.2.1   Fabrication of microheater layer

The first step of the sensor fabrication was to make the micropattern utilised for Joule heating. The substrate was prepared through a cleaning process where it was placed in a $130\,^\circ$C 2:1 solution of sulphuric acid and hydrogen peroxide, for 10 minutes. To protect the side of the substrate which would not be covered by platinum, it was spin coated by MMA(8.5)MAA copolymer resist during 1 minute, using a spinning velocity of 3000 rpm, followed by softbaking at $180\,^\circ$C for 10 minutes. The other side of the substrate was first covered by hexamethyldisilazane (HMDS) to promote resist adhesion and subsequently spin coated by LOR-3A using a spinning velocity of 3000 rpm for 1 minute, followed by softbaking at $180\,^\circ$C for 10 minutes. A second photoresist, S1805, was then spin coated on the surface, using the same spinning velocity but instead for 30 seconds, followed by softbaking at $110\,^\circ$C for 3

minutes.

Subsequently, the double resist layer was laser exposed according to the microheater pattern, using a *Heidelberg Instruments DWL 2000* laser writer. Then the resist was developed in MF319 for 2 minutes, followed by rinsing in deionised water and blow drying. The bottom photoresist layer of LOR-3A has a faster developing rate compared to the upper photoresist layer of S1805, hence there was a gap between the substrate and upper photoresist layer which ensured improved lift off quality. The surface was then exposed to an oxygen plasma for 15 seconds, followed by the evaporation of 10 nm Cr and 100 nm Pt with a *Lesker PVD 225* evaporator. Finally, a lift off procedure was performed where the sample was emerged in the remover mr-Rem 400 overnight and then rinsed by isopropyl alcohol (IPA) and deionised water, before being blow dried.

3.2.2 Hole-colloidal lithography

In order to fabricate the array of gold nanodiscs on the sensors, HCL was preformed. First the wafer was cleaned by ultrasonication for 10 minutes respectively in acetone and IPA, followed by exposure to oxygen plasma for 5 minutes on the side opposite to the metal layer. Poly(methyl methacrylate) (PMMA) was then spin coated on the surface, using a spinning velocity of 2000 rpm for 1 minute, followed by soft baking at 170 °C for 10 minutes. In order to hydrophilise the surface, the PMMA layer was subsequently oxygen ashed for 5 seconds. Positively charged poly(diallyldimethylammonium) chloride (PDDA) was then pipetted on the surface and rinsed off the surface with deionised water after 45 seconds. The same process was then repeated with a solution of negatively charged polystyrene (PS) beads having diameters of 120 nm, but the time interval before rinsing was instead 3 minutes. Due to the opposite charge of the polymers, the PS beads were attached to the surface with high adhesion. A 20 nm layer of chromium was then evaporated on the surface with *Lesker nano Cr* evaporator, followed by tape stripping of the Cr-covered PS beads, resulting in a hole mask. The surface was then exposed to an oxygen plasma for 5 minutes in order to ash through the exposed PMMA layer. Subsequently, a 20 nm Au layer was evaporated on the surface with a *Lesker PVD 225* evaporator, followed by lift off in acetone which resulted in the Cr hole mask being removed and only Au discs remaining.

3.3 Wire bonding of multiplexing sensors

As the ordinary contact electrodes would be too large to supply electric power to the different regions on the multiplexing sensors, each multiplexing sensor had to be wire bonded to a printed circuit board (PCB) designed specifically for said sensor. This was done by first using an epoxy glue to attach the sensors to the PCB, followed by the actual wire bonding which connects the microheater regions to metal pads on the PCB. The PCB:s have circular holes on the positions where the spiral areas will be positioned, which allows air to reach the sensing areas.

3.4   Characterisation of the microheaters

To determine the TCR of the microheaters, the device with the sensor inserted, was put in an oven with a temperature set to $50\,°\mathrm{C}$. While the device was heated from room temperature, the resistance along with the temperature (measured by a secondary RTD in the device, with a known bulk temperature coefficient) was measured every second. The resistance ratio was then linearly fit against the temperature as

$$\frac{R}{R_0} = \alpha T + (1 - \alpha T_0) \tag{3.1}$$

in order to obtain the temperature coefficient from the slope of the graph.

To determine the power consumption required to heat the different micropatterned sensors, the voltage supply to the microheater was set to some different values while the resistance was simultaneously measured. By using the previously measured temperature coefficient, as well as Ohm's law, the power consumption and sensor temperature was calculated for these measurement points. For some of the multiplexing sensors, the resistance was also simultaneously measured in the other active regions with a multimeter while one of the regions was heated. This allowed an estimation of the resulting temperatures in the other regions, and hence of the heat spread on the sensor.

Additionally, the temperature distributions on the sensors were analysed by thermal imaging, using a *Fluke Ti400* IR-camera. The surface emissivity used during the measurements was chosen to be 0.94, i.e. the same value used in the model for the glass substrate.

4

Results and discussion

4.1 Sensors with a single active region

In sections 4.1.1-4.1.2 the modelling results regarding the current microheater designs, as well as the tested modifications to this model, are shown and discussed. These results, together with practical aspects, were the motivation for the fabricated microheater designs that are described in section 4.1.3. Note that from now on, the sensor side with the microheater layer will be referred to as the frontside while the sensing side will be referred to as the backside.

4.1.1 Modelling of the current microheater design

For the model of the current microheater, the needed electrical power to achieve a maximum temperature of 120 °C on the sensor is approximately 0.145 W. The resulting temperature profile on the front and back of the microheater, when applying this power, can be seen in figure 4.1a. As seen in the figure, the temperature profile on the backside of the spiral area is relatively uniform, but approximately 15 °C lower than that of the front of the spiral area. In figure 4.1b, the maximum temperature on both the front- and backside of the modelled microheater can be seen as a function of the applied power. As noticeable from the figure, the difference between the maximum temperatures of the front- and backside increases with increasing power. In other words, even though the temperature difference is negligible for NPS for the current heater temperature of 120 °C, this is probably not the case if a higher temperature would be needed. In that case, the front side of the microheater would need to be heated unnecessarily high in order to compensate for the temperature drop on the backside, which would be energy inefficient. Hence, a goal for the new microheater designs is that the temperature difference between the two sides should remain small, even at high temperatures.

(a)

(b)
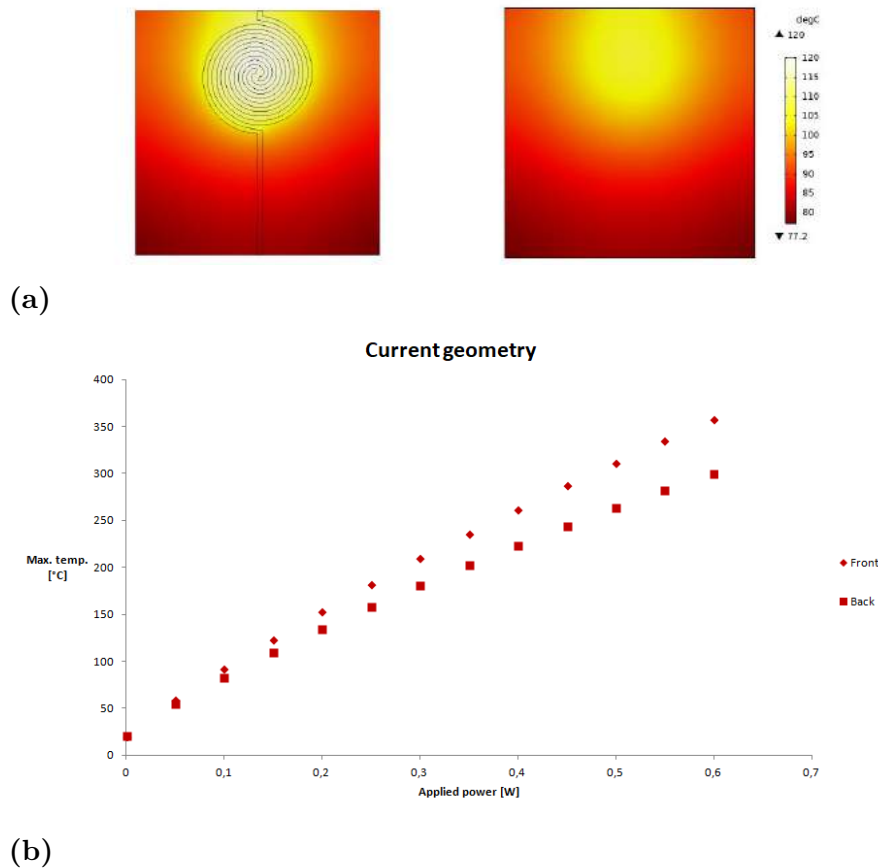
Figure 4.1: (a): The temperature profile of the front- and backside of the modelled current microheater, when the applied power is 0.145 W. **(b)**: Maximum temperature on the front- and backside, as a function of applied power.

4.1.2 General modifications for energy optimisation

In order to find potential ways to decrease the energy consumption of the device, several alterations have been made to the model for the current microheater, as seen below. For a summary of the given modifications to the microheater and how much they decrease the energy consumption, see table 4.4.

4.1.2.1 Reduced substrate thickness

In figure 4.2, the maximum temperature on the front- and backside of the sensor can be seen as a function of applied power, for some different substrate thicknesses. It is apparent from the graph that a thinner substrate yields two benefits, both that the overall power consumption is reduced, but also that the temperature drop between the front- and backside is reduced. This is expected, since a lower substrate thickness means both a smaller mass to heat up and a shorter heat conduction distance between the front- and backside. To specifically reach a maximum temperature of 120 °C on the frontside, 0.115 W is required with a 0.5 mm substrate and 0.081 W with a 0.2 mm substrate. This corresponds to a decrease in power consumption of about 21 % and 44 %, respectively.
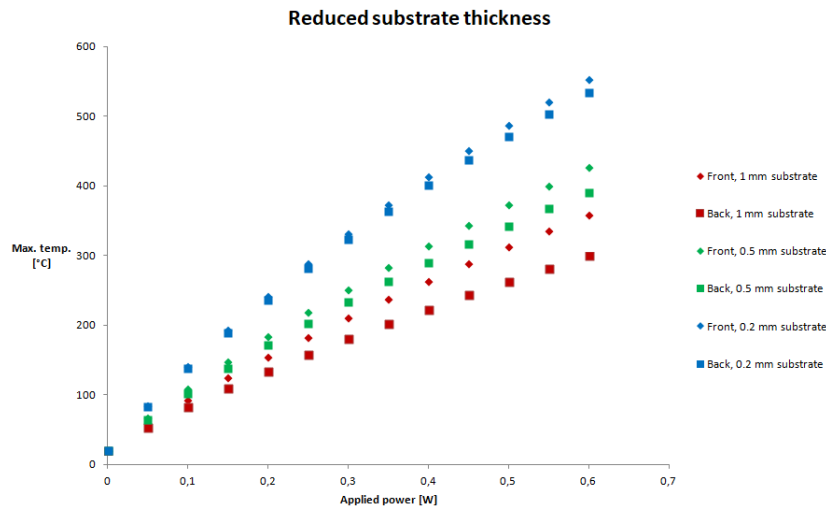
Figure 4.2: Maximum temperature on the front- and backside as a function of applied power, when the substrate thickness is 1 mm (current sensor), 0.5 mm and 0.2 mm.

4.1.2.2 Scale down of sensor chip

A further step than just reducing the substrate thickness is to scale down the entire sensor chip, which is presented in figure 4.3 where the power consumption change due to a scale down of 50 % and 80 % are compared to the current sensor. In comparison to just reducing the substrate thickness, as seen in figure 4.2, doing a full scale down has a much larger effect on the power consumption. However, reducing the dimensions of the sensor also leads to more complicated handling of the chip and will make it impossible to use the present electrodes in the device. Additionally, a scale down means that less light will reach the detector since the spiral area is decreased, which could have consequences. To reach a maximum temperature of 120 °C on the frontside of the sensor, approximately 0.054 W is needed when the sensor is scaled down by 50 %, and 0.0153 W for a 80 % scale down. This corresponds to a relative decrease in energy consumption of about 63 % and 90 %, which is a much greater change compared to just altering the substrate thickness, as expected.
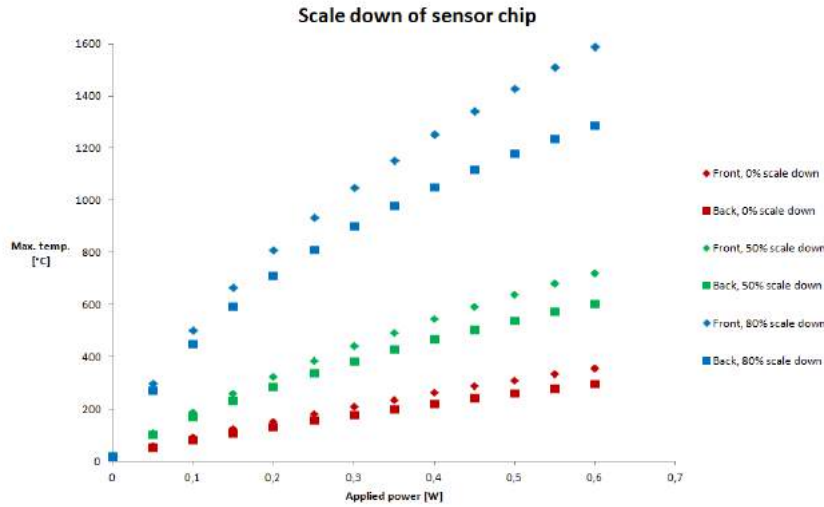
Figure 4.3: Maximum temperature on the front- and backside as a function of applied power, when the sensor is scaled down by $0\,\%$ (current sensor), $50\,\%$ ($2.5\,\text{x}\,2.5\,\text{x}\,0.5\,\text{mm}$ sensor) and $80\,\%$ ($1\,\text{x}\,1\,\text{x}\,0.2\,\text{mm}$ sensor).

4.1.2.3 Spiral geometry

In figure 4.4, the temperature profile of the microheater can be seen when altering the number of turns in the spiral or the the air gap width. In the case with fewer turns or wider air gap, the needed power to achieve a maximal temperature is decreased slightly, which might be due to a small difference in the temperature profile. However, these changes are in principle negligible. Rather, the factor of interest that is affected more considerable is the electrical resistance of the microheater, which is expected from equation 2.5, since the wire width and/or length is affected in the four cases. The resistance changes and spiral geometry parameters are presented in table 4.1. As noticeable from the table, the changes in the spiral length-width ratio L/w, corresponds very well to the change in the modelled resistance, between the different cases. Since a smaller electrical resistance is desired to lower the voltage over the microheater according to Ohm's law, it might be relevant to have fewer spiral turns and/or a smaller air gap in the microheater. It is also possible to achieve a lower resistance by increasing the metal layer thickness, according to equation **??**, but this is limited by the metal-substrate adhesion. Note that alternative geometries to the circular double spiral have been briefly investigated in appendix A.1.

(a)

(b)
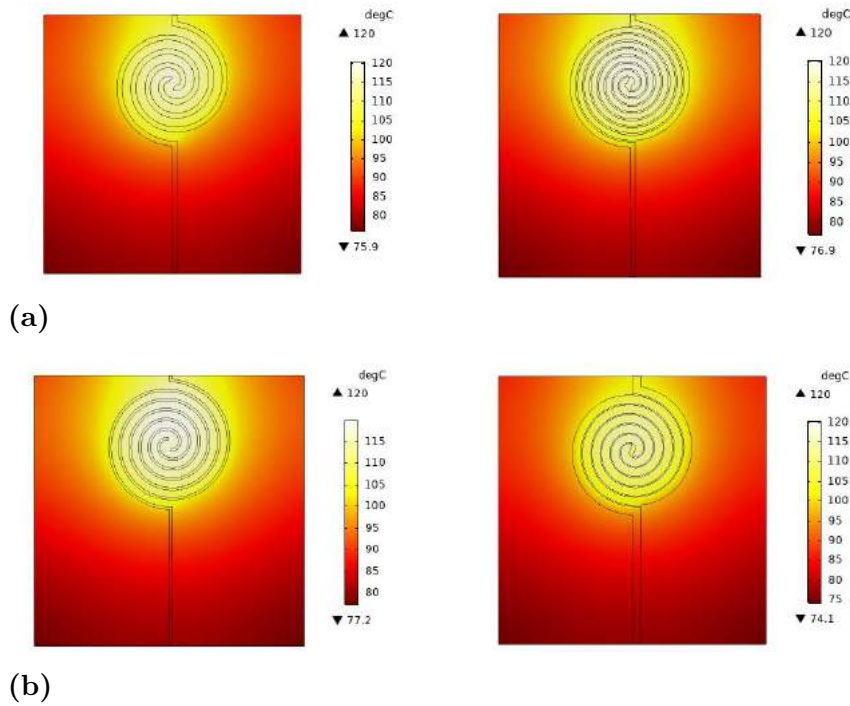
Figure 4.4: (a): Temperature profile for the microheater with less (left) and more (right) spiral turns compared to the original heater geometry. In the case with less turns, 0.140 W is applied, while 0.145 W is applied in the case with more turns. **(b)**: Temperature profile for the microheater with 50 % reduced (left) and 50 % increased (right) air gap width. In the case with a thinner air gap, 0.145 W is applied, while 0.136 W is applied in the case with wider air gap.

Table 4.1: The spiral geometry parameters, as well as the modelled resistance, for the four different spiral geometries displayed in figure 4.4.

Case	Wire width w [μm]	Wire length L [mm]	L/w	Modelled resistance [Ω]
Current geometry	72	21	292	203
Decreased number of spiral turns	162	14	86	59
Increased number of spiral turns	26	28	1077	744
Air gap width reduced by 50 %	127	23	181	122
Air gap width increased by 50 %	17	19	1117	816

4.1.2.4 Spiral position

In the current sensor, the spiral area is located near the chip border, and it might therefore be useful to see if and how the temperature profile and power consumption

is affected by centralising the spiral, which can be seen in figure 4.5. In order to reach a maximum temperature of 120 °C, the required power is 0.150 W, which is slightly higher than the current power consumption of 0.145 W. This small increase is likely due to the spiral area being further from the chip border, where the heat conduction instead occurs to air, which has a much lower heat conductivity than glass and platinum. However, this relative increase is so low (approximately 3 %) that it overall is negligible.
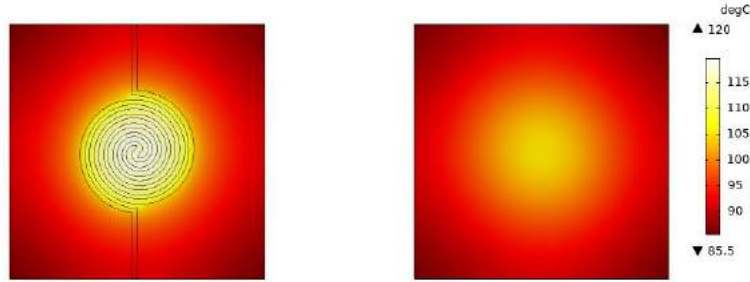
Figure 4.5: Temperature profile on the front and back of the microheater when the spiral area has been centralised and the applied power is set to 0.150 W.

4.1.2.5 Spiral size

Another interesting alteration is to change the size of the spiral area. In figure 4.6a the temperature profile of the front- and backside can be seen of a sensor with 50 % lower spiral diameter and air gap width, when 0.111 W is applied. Reversely, in figure 4.6b, the front- and backside temperature profile can be seen when 0.175 W is applied to a sensor with 50 % increased spiral radius and air gap width, which also is centralised in order for it to fit on the chip. These two cases then, respectively, corresponds to a decrease of 23 % and increase of 21 % to the power consumption. Furthermore, in figure 4.6c the maximum temperature on the front- and backside can seen on both these modelled sensor types as a function of applied power. As noticeable from the figures, while a smaller spiral area leads to a smaller power consumption to reach a certain sensor maximum temperature, the relative temperature difference between the front- and backside also increases drastically. This means that it would be impossible to have 50 % spiral radius with the current sensor dimensions, but it could potentially show promise in case the substrate thickness is decreased simultaneously. For an increased spiral radius, the temperature drop to the backside of the sensor is decreased, but the overall power consumption is increased. As discussed previously, one must also consider the practical consequences of altering the size of the sensor's active region.
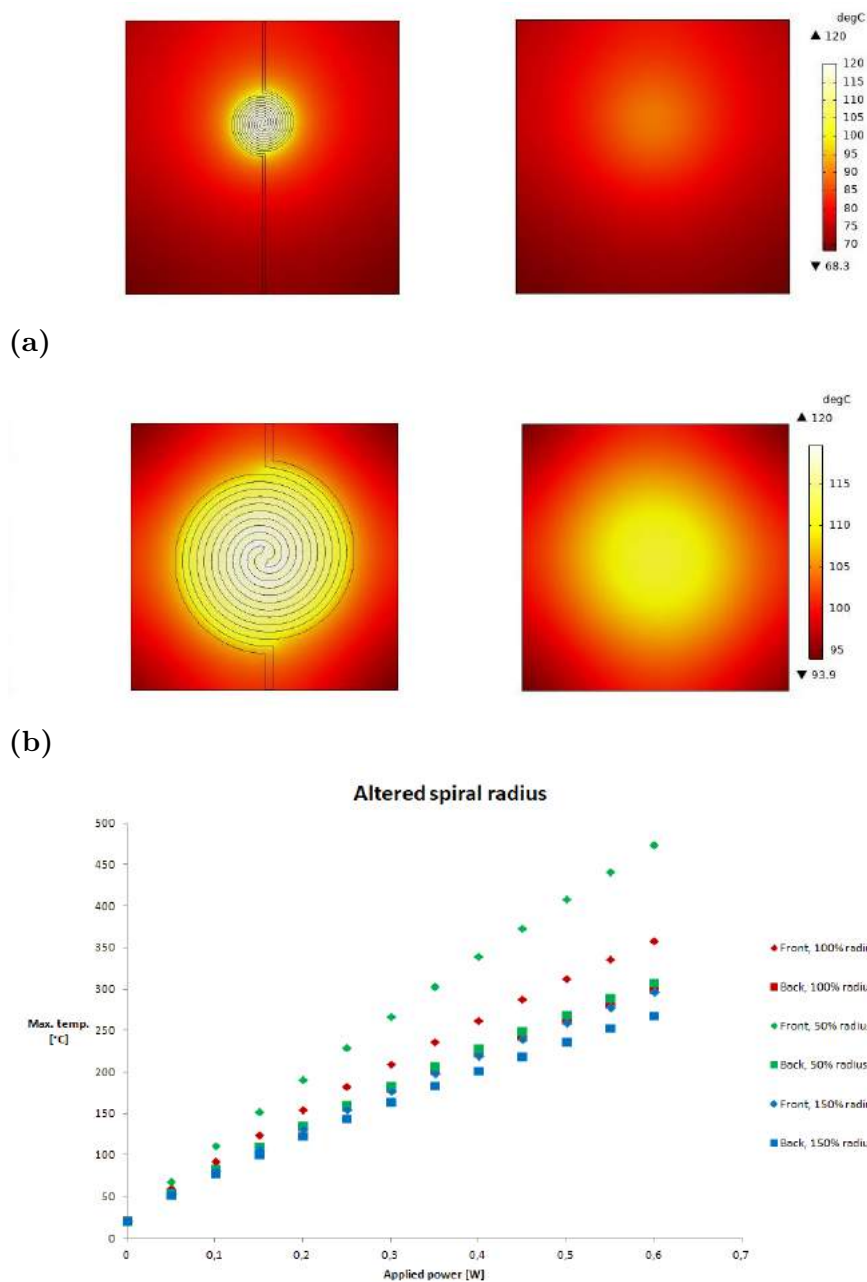
(a)

(b)

(c)

Figure 4.6: (a): The temperature profile of the front- and backside of the modelled microheater with a $50\,\%$ reduced spiral radius, when the applied power is $0.111\,\mathrm{W}$. **(b)**: The temperature profile of the front- and backside of the modelled microheater with a $50\,\%$ increased spiral radius, when the applied power is $0.175\,\mathrm{W}$. **(c)**: Maximum temperature on the front- and backside, as a function of applied power, when the spiral radius is altered.

4.1.2.6 Sensor with grooves

By some process, e.g. dicing, etching or cutting by laser, it is possible to make a groove in the sensor. In figure 4.7, two different cases with grooves are compared.

In the first case, there are three straight grooves on the backside with a depth of 0.8 mm and a width of 0.22 mm. In the second case, the spiral area is enclosed by a ring-shaped groove on the backside, which also has a depth of 0.8 mm and width of 0.22 mm. To reach the temperature profiles shown in figures 4.7a,b , 0.120 W and 0.118 W need to be applied, respectively. This corresponds to a power decrease of 17 % and 19 %. In other words, both sensor geometries consume almost the same power, which also can be deduced from figure 4.7c. Compared to the current sensor, both the power consumption and relative temperature difference between the front- and backside of the microheater, are decreased. Additionally, the temperature profile uniformity of the active region seems to be somewhat improved. Note that in reality, the grooves would likely not be as perfect as they are depicted in these images, but that is assumed to overall have a low implication on these factors. Furthermore, as seen in tables 4.2 and 4.3, increasing groove depth and/or width will lower the power consumption in both cases.

(a)

(b)

(c)
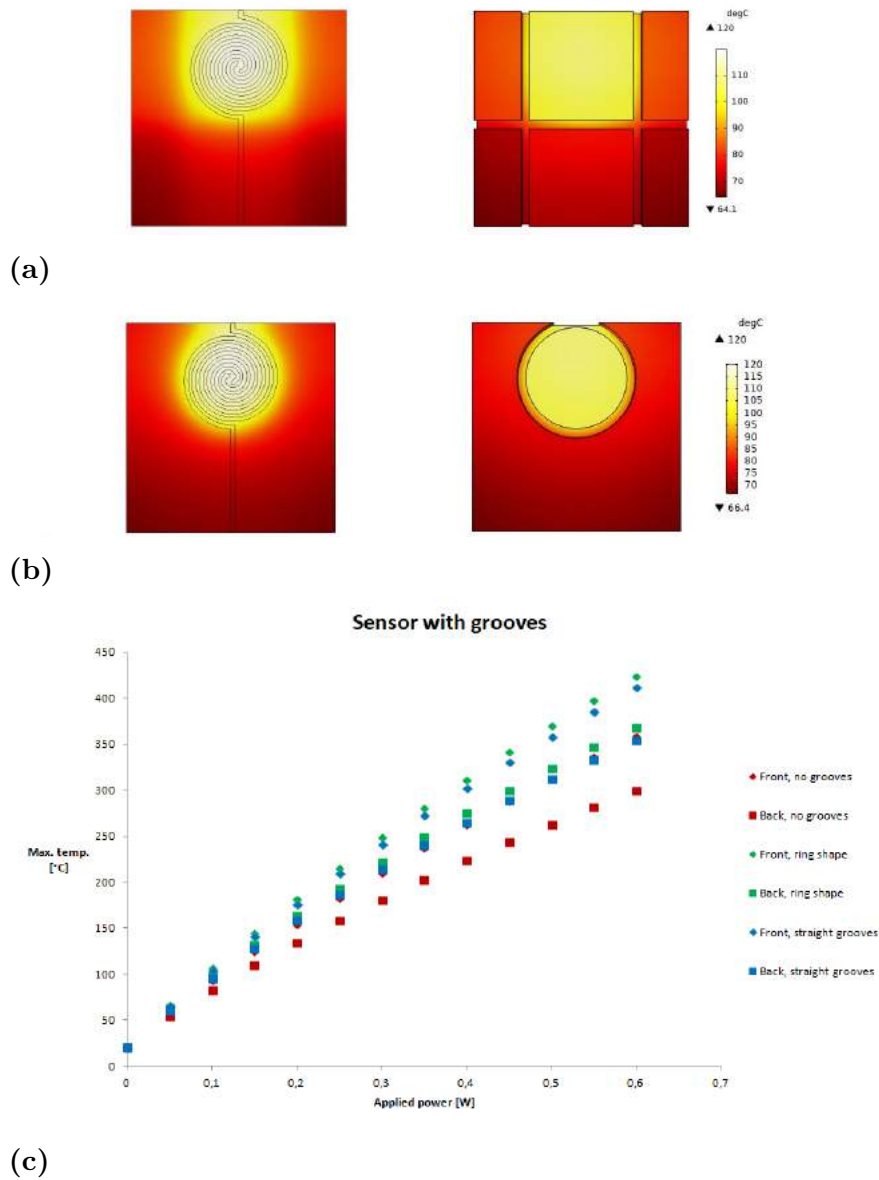
Figure 4.7: (a): The temperature profile of the front- and backside of the modelled microheater with three straight grooves on the backside, when the applied power is 0.120 W. **(b)**: The temperature profile of the front- and backside of the modelled microheater with a ring-shaped groove on the backside, when the applied power is 0.118 W. **(c)**: Maximum temperature on the front- and backside, as a function of applied power.

Table 4.2: Maximum temperature (in °C) on the sensor with a ring shaped groove, when 0.118 W is applied and the groove width and/or depth is varied.

width depth	0.11 mm	0.22 mm	0.33 mm	0.44 mm
0.2 mm	103.9	104.5	104.9	105.3
0.4 mm	105.6	106.7	107.4	108.9
0.6 mm	108.8	111.0	112.2	113.5
0.8 mm	116.3	120.3	123.2	125.9

Table 4.3: Maximum temperature (in °C) on the sensor with straight grooves, when 0.120 W is applied and the groove width and/or depth is varied.

width depth	0.11 mm	0.22 mm	0.33 mm	0.44 mm
0.2 mm	105.8	106.5	107.1	107.5
0.4 mm	107.5	108.6	109.4	110.2
0.6 mm	110.5	112.1	113.6	114.8
0.8 mm	116.8	119.7	122.0	124.1

4.1.2.7 Laser cut designs

If the substrate is sufficiently thin, e.g. 0.2 mm or below, it is possible to use a laser to cut the sensor in specific shapes. Examples of such shapes can be seen in figure 4.8a, where the temperature profile of the frontside can be seen for four different laser cut designs. The temperature profile on the backside are not shown for these cases, due to it being almost identical to the one on the frontside, which can be understood from figure 4.8b. It is interesting here to note that, according to figure 4.8b, the temperature of design 1 and design 2 have almost the same power dependence (it is impossible to separate them from the graph alone), and design 4 has only a slightly higher power consumption. This indicates that one of the determining parameters for power consumption of these designs, is how well connected the spiral area is to the remaining substrate, i.e. the shared width between these, which is approximately the same for design 1 and 2, and slightly larger for design 4. If conduction is the determining heat transfer mechanism, this is not surprising, since this factor determines how well the heat can conduct from the spiral to the remaining area. The limited heat conduction also leads to improved temperature uniformity along the active region.
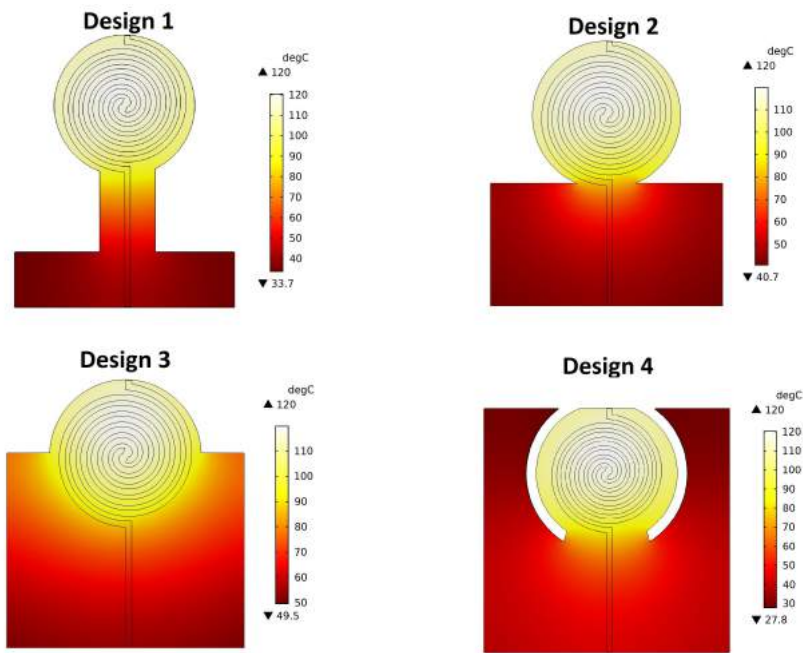
(a)
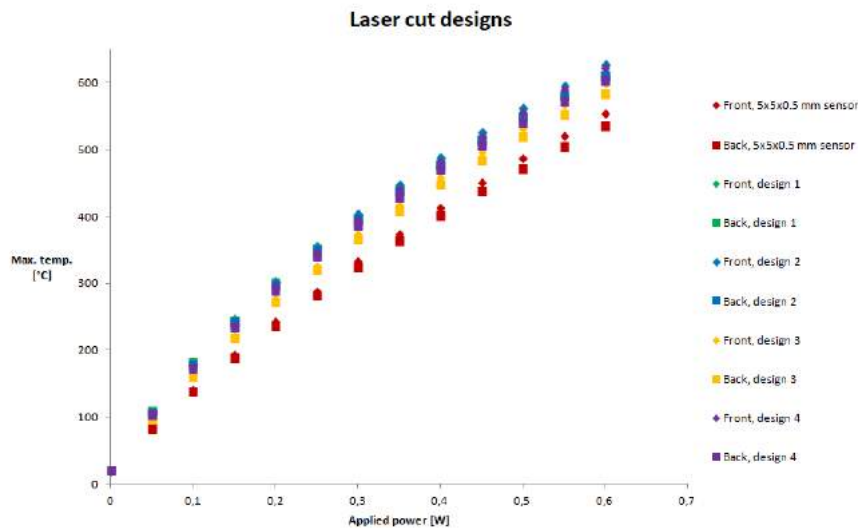
(b)

Figure 4.8: (a): The frontside temperature profile of a 0.2 mm thick sensor, when it is cut into four different designs by e.g. a laser. From design 1 to 4, the applied powers are 0.057 W, 0.058 W, 0.067 W and 0.061 W. **(b)**: Maximum temperature on the front- and backside, for these four different designs. The measurement points for design 2 are behind the measurement points for design 1. Note that they are compared to a 5 x 5 x 0.2 mm sensor and not the 1 mm thick sensor geometry.

4.1.2.8 Summary

In table 4.4, the energy consumption of the microheater in the different cases investigated in section 4.1.2 can be seen, as well as their relative change in power consumption compared to the current microheater. Simply comparing the relative change in power consumption, scaling down the sensor is the most promising alteration. However, as mentioned earlier, this has practical complications.

Table 4.4: The different modifications done to the model of the current microheater and how the power consumption to reach a maximum temperature of 120 °C is altered as a result.

Modelled case	Power consumption [W]	Relative change [%]
Current microheater	0.145	0
Substrate thickness reduced by 50 %	0.115	-21
Substrate thickness reduced by 80 %	0.081	-44
50 % scale down of sensor	0.054	-63
80 % scale down of sensor	0.015	-90
Decreased number of spiral turns	0.140	-3
Increased number of spiral turns	0.145	0
Air gap width reduced by 50 %	0.145	0
Air gap width increased by 50 %	0.136	-6
Spiral centralised	0.150	+3
Spiral radius reduced by 50 %	0.111	-23
Spiral area centralised and spiral radius increased by 50 %	0.175	+21
Straight grooves (0.22 mm width, 0.8 mm depth)	0.120	-17
Circular groove (0.22 mm width, 0.8 mm depth)	0.118	-19
Laser cut design 1	0.057	-61
Laser cut design 2	0.058	-60
Laser cut design 3	0.067	-54
Laser cut design 4	0.061	-58

4.1.3 Fabricated sensors with a single active region

For sensors with a single active region, five new designs were fabricated, investigated and compared to the former design, which from now on is referred to as design (a), while the new designs are referred to as designs (b)-(f). Design (b) utilised the same dimensions as design (a), but it also had a circular laser cut groove on the backside, with an approximate depth and width of 0.5 mm and 0.2 mm. Design (c), as well as designs (d)-(f), had a reduced substrate thickness of 0.175 mm. Design (d) also utilised an active region with approximately half the spiral diameter, i.e 1.2 mm. Design (e) had the original spiral diameter, but the spiral wire was both wider and shorter. Design (f) had the same dimensions as design (c), but it also had a laser cut gap which was approximately 0.1 mm wide. The new sensors, along with the previous sensor, can be seen in figure 4.9. The measured power and voltage requirement to reach 120 °C, the resistance at 120 °C, as well as the TCR obtained from calibration for each sensor, can be seen in table 4.5. The calibration graphs to find the TCR:s, as well the graphs showing the relationship between power consumption

and temperature for the different sensors, can be found in appendix A.2.

There are several things of interest to note from table 4.5. First off, the TCR value vary surprisingly much between the different sensors, despite the platinum layer being fabricated through the same method and having roughly the same thickness. It remains unclear if this is due to some of the sensors being fabricated in different batches, or if it can be explained by an inaccurate calibration method. Note that if these TCR values would be incorrect, it would also lead to an incorrect relationship between microheater power consumption and resulting temperature.

Regarding the power consumption, design (d) show the greatest improvement with a power decrease of roughly 51 %. However, the power consumption change for design (d), as well as for the other designs (except for design (b)), was excepted to be larger. For design (f), one explanation might be that it is incorrect to model the air in the gap as normal air. Due to the gap being as thin as roughly 0.1 mm wide, the air flow might be so constrained that it in principal is completely stagnant, which would yield a higher thermal conductivity and hence a higher required power consumption. This could possibly be resolved by instead modelling the air as a solid instead of a gas, in this gap region. For the other designs, it is however unknown what could be the cause for the large deviance between the actual and modelled values. For design (a), the indicated power consumption by modelling was 0.145 W as reported in section 4.1.1, which is 34 % lower than the measured value. This error is likely due to the approximations described in section 3.1. If this error is not constant and instead varies between the different designs, it could also explain the discrepancy between actual and modelled power consumption, when comparing design (a) with the remaining ones.

It should also be noted that only the temperatures on the frontsides of the sensors have been investigated, as it is that temperature that is obtained from the thermoresistive measurements. As indicated by the simulations, the temperature is likely lower on the backside of the sensor, even though this likely is improved by utilising a thinner substrate. Hence, this is a benefit of designs (c)-(f) that is not properly accounted for in table 4.5.
For design (e), the intended outcome was to significantly lower the resistance, which has been achieved as it is measured to be 74-80 % lower than that of the other sensors, and as also seen from table 4.5, design (e) could almost be driven by a 3 V battery. The power consumption was still expected to be the same or very close, for design (c) and (e), as only the spiral geometry differ between these. Yet, they do differ with 6 percentage points. This probably indicates that there are differences in the temperature distribution which cause the latter to have a slightly higher power consumption. Regarding the resistance for the other designs, they are quite similar. Design (a) and (f) do, however, show a higher resistance compared to design (b)-(d), which might indicate that these designs have different film thickness and/or film quality, which could also explain why the TCR differ between these.

Thermal images of the front- and backsides of the different sensors, when the max-

imum temperature is approximately 120 °C, can be seen in figure 4.10 and 4.11, respectively. As noticeable from figure 4.11, the centre of the active region is approximately 15-25 °C higher than at the periphery, for all sensors. Design (b) and (f) show, as expected, a great increase in temperature uniformity on the backside of the sensors. The other thin sensors, i.e. design (c)-(e), also show a more localised high temperature region, compared to design (a). This is likely due to the fact that it is harder for the heat to spread laterally if the conduction distance between the front- and backside is decreased. Figure 4.11 also shows that the contact electrodes has a significant effect on the temperature profile, and hence also likely on power consumption, for the different sensors. This is most easily seen in design (a)-(b), where the temperature gradient seem to be evidently increased downward towards the contacts.
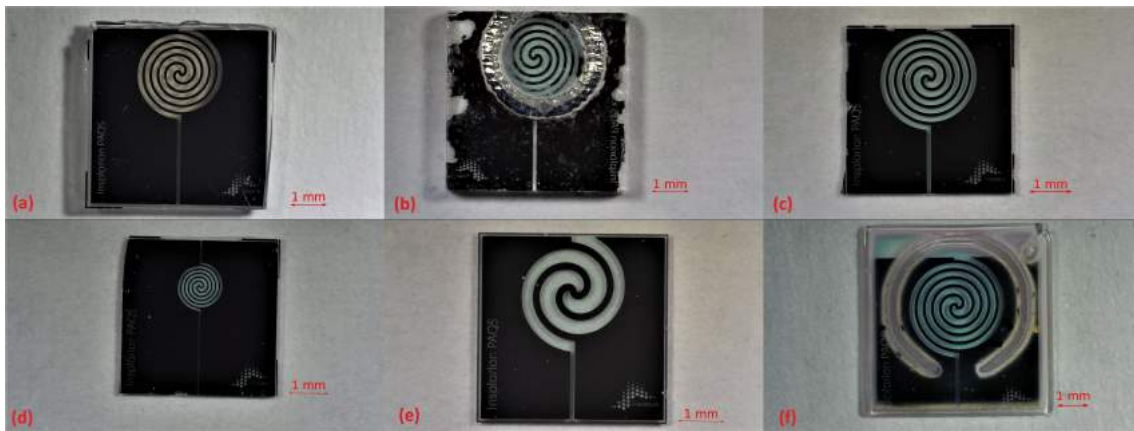
Figure 4.9: The different tested sensors with a single active region. **(a)**: Previous sensor design. **(b)**: 5 mm thick sensor with a 0.5 mm deep and 0.2 mm wide laser cut groove on the backside. Note that the backside of the sensor is upwards in the image to show the groove. **(c)**: 0.175 mm thick sensor. **(d)**: 0.175 mm thick sensor with half the spiral diameter. **(e)**: 0.175 mm thick sensor with an alternative spiral geometry where the spiral wire is both wider and longer. **(f)**: 0.175 mm thick sensor with a 0.1 mm wide laser cut gap.

Table 4.5: Tested properties of the different sensors. The design numbering refers to the one shown in figure 4.9. *Note that for the modelled power consumption change, models for each of the designs were made, except for design (e) due to its exact spiral geometry being complicated to model. Instead design (e) was assumed to have the same power consumption as design (c), since they had the same substrate thickness and roughly the same spiral size. However, as their temperature profile might differ due to having different spiral geometries, the actual power consumption might differ slightly, which is observed in the experimental results.

Sensor	TCR $[K^{-1}]$	R(120 °C) $[\Omega]$	U(120 °C) [V]	P(120 °C) [W]	Relative consumption change [%]	Modelled consumption change [%]
Design (a)	0.0024	259.95	7.55	0.219	0	0
Design (b)	0.0027	202.72	6.43	0.204	-7	-6
Design (c)	0.0028	205.17	5.72	0.159	-27	-47
Design (d)	0.0027	203.00	4.66	0.107	-51	-60
Design (e)	0.0026	53.10	3.02	0.172	-21	-47*
Design (f)	0.0023	259.37	6.17	0.147	-33	-60
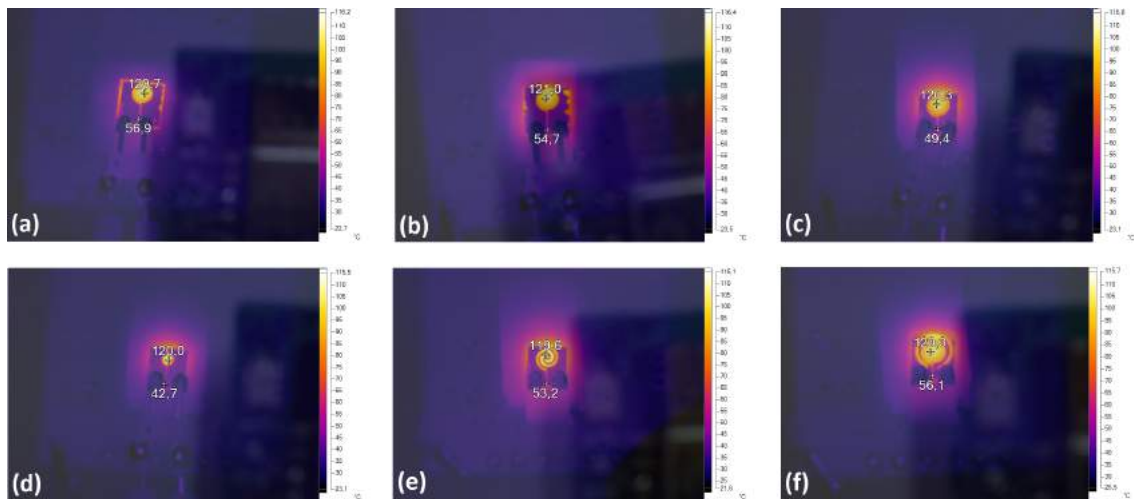
Figure 4.10: Thermal images of the frontsides of the different sensors when the voltage is adjusted such that the maximum temperature on the sensor is approximately 120 °C, where the temperature scale is in °C. The design numbering is the same as in figure 4.9. Note that the metal layer temperature is not according to the scale, due to having a much lower surface emissivity than the glass.
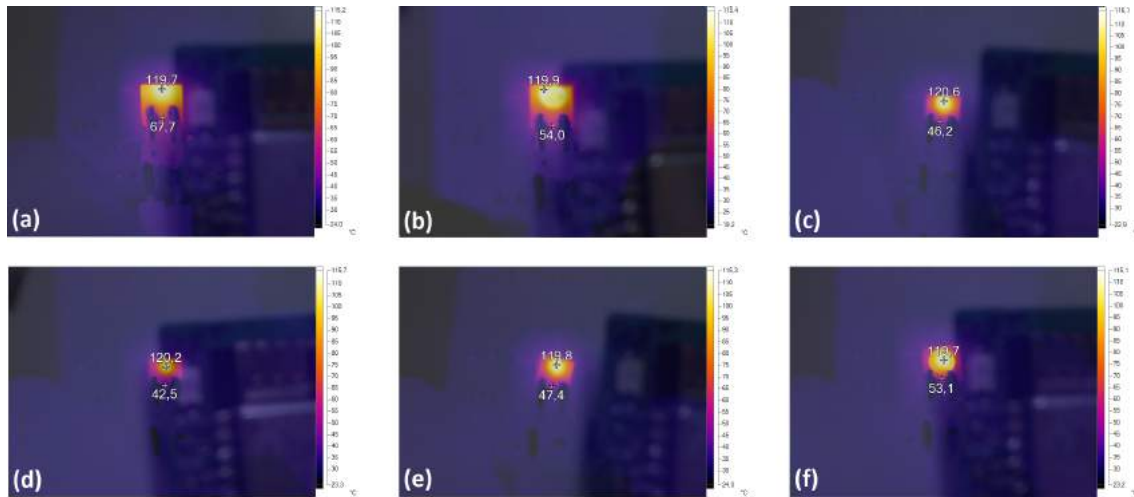
Figure 4.11: Thermal images of the backsides of the different sensors shown in figure 4.10, where the temperature scale is in °C. Note that the voltage is adjusted such that the shown maximum temperature is roughly 120 °C, i.e. a different voltage and power is applied than in figure 4.10.

4.2   Multiplexing

For multiplexing, two options were considered. In the first option, each gas would be sensed using an individual chip with a specific SMO coating and held temperature, chosen to sense a specific gas. It could then be assumed that the sensors would not affect each other, i.e. the power consumption of each individual sensor would be the similar to those studied in section 4.1. The second option, which has been studied more explicitly, is that the different sensing regions would be on the same chip. Though this is a more space efficient alternative, this also requires a sensor design which is able to maintain distinct temperature regions. Note also that depositing several different SMO:s on the same sensor, on different regions, will require a more complex fabrication process.

In section 4.2.1, three different multiplexing designs are modelled, which later were fabricated and characterised, as shown in section 4.2.2. For the sake of this project, it has been assumed that there will be four different sensing regions on the multiplexing chips.

4.2.1   Modelled alternatives for multiplexing

In figure 4.12, three different multiplexing designs can be seen which respectively are referred to as multiplexing design (1), (2) and (3). All these designs have a chosen substrate thickness of 0.175 mm and spiral diameters of 1.22 mm, in order to obtain the low energy consumption which was exhibited by design (d) in section 4.1.3. For multiplexing design (1) and (2), each active region has its own electric source and

ground, while multiplexing design (3) has an unified ground for all four active regions. Regardless, for all three designs it is then possible to individually control the current supply to each region and hence to some degree also individually control the resulting temperatures. However, by heating one region the temperatures of the remaining ones will likely be affected. This has been investigated further in figures 4.13-4.15, where two cases have been modelled for each design. In the first case, power is applied to one of the regions such that its maximum temperature is 120 °C. In the second case, a "worst case" scenario was investigated, in which the same power is applied to three different regions, such that the maximum temperature of the sensor is 300 °C. Additionally, figures 4.13-4.15 also show two graphs each which generalises both cases, as they show the modelled temperature in each region when either one or three of the regions are heated with a certain power. Note that it is not currently known what the optimal temperatures would be to measure other gases than NO_2, which means that different regional temperatures on the same sensor could be required to vary from below 120 °C to above 300 °C.

Comparing multiplexing design (1) and (2), design (2) has a lower heat spread between the different active regions due to a larger distance between the spiral regions. However, multiplexing design (2) is consequently less power efficient than multiplexing design (1), since it has more excess mass which can conduct heat. In other words, by increasing the sensor area there is a trade-off between temperature localisation and energy efficiency. Furthermore, a larger sensor is less space efficient and might be more prone to breaking when handling.

For multiplexing design (3), the geometry has a high aspect ratio in contrast to the previous designs. Subsequently, the distance between two neighbouring regions is shorter than in multiplexing design (1), while at the same time the distance between the two edge regions exceeds the distance between two opposite regions in multiplexing design (2). Hence, when comparing the "worst case scenario" between the three designs, only multiplexing designs (2) and (3) manage to keep the minimum temperature below 120 °C. According to the graphs in figures 4.14c and 4.15c, the three heated regions has to reach temperatures near 500 °C before the non-heated region reach 120 °C, both in design (2) and (3), which seems very promising. However, multiplexing design (3) still has more prominent heat spread between two neighbouring regions, compared to multiplexing design (2). This means that multiplexing design (3) might be less suitable if there are several regions that require a low temperature, instead of only one.
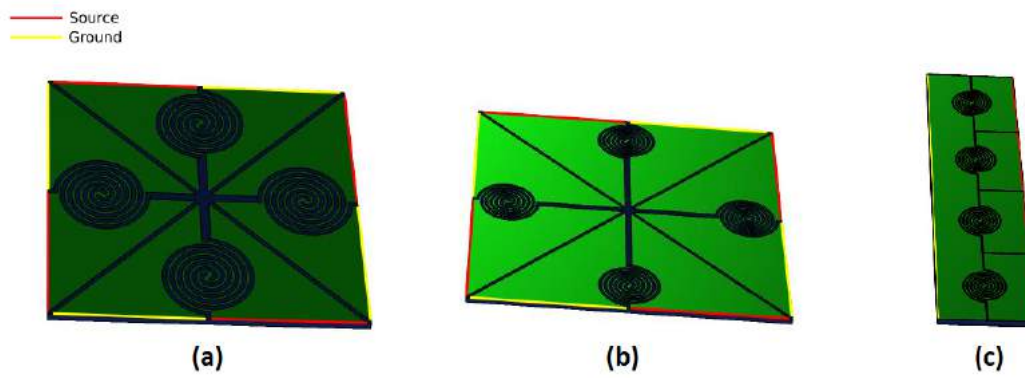
Figure 4.12: Three different multiplexing designs, where the electric sources are highlighted in red and the grounded edges are highlighted in yellow. For all designs, the spiral areas have diameters of 1.22 mm. **(a)**: Multiplexing design (1), a 5 x 5 x 0.175 mm sensor. The distances between the spiral regions are; 2.60 mm and 3.73 mm. **(b)**: Multiplexing design (2), a 7.5 x 7.5 x 0.175 mm sensor. The distances between the spiral regions are; 4.37 mm and 6.23 mm. **(c)**: Multiplexing design (3), a 10 x 2.5 x 0.175 mm sensor. The distances between the spiral regions are; 2.5 mm, 5 mm and 7.5 mm.
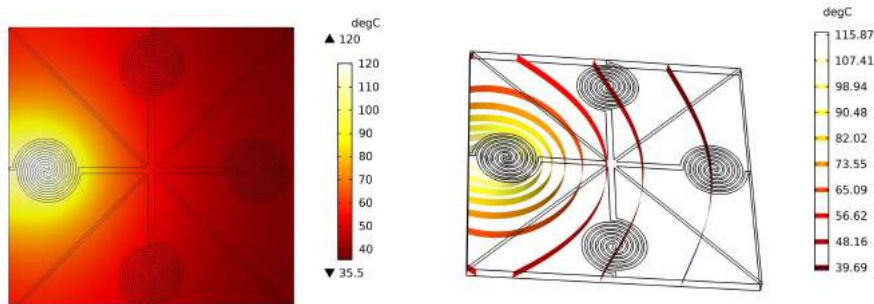
(a)
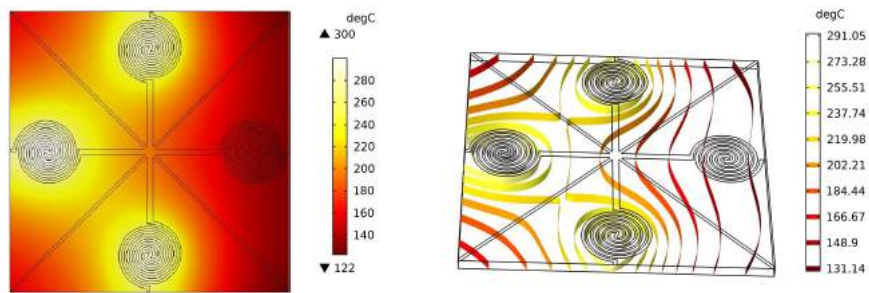
(b)
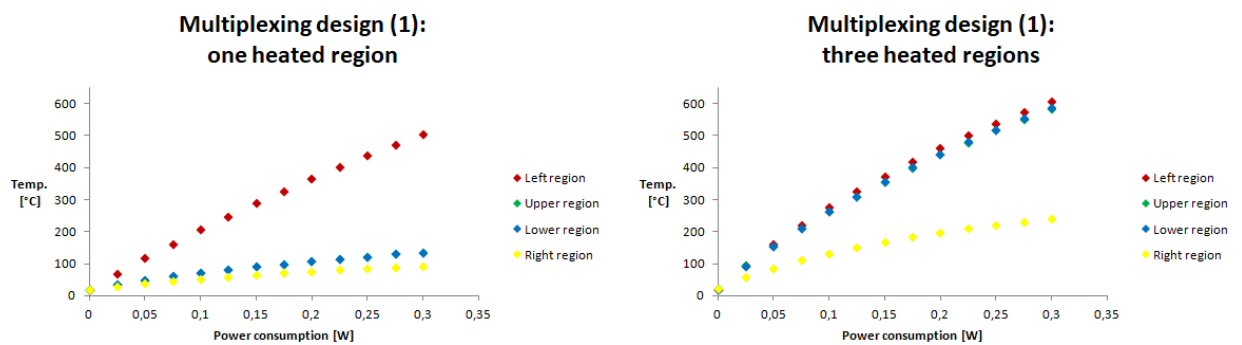
(c)

Figure 4.13: **(a)**: Temperature profile (left) and isothermal contours (right) for multiplexing design (1), when 0.049 W is applied to the left microheater region, resulting in a maximum temperature of 120 °C on the chip. **(b)**: Temperature profile (left) and isothermal contours (right) for multiplexing design (1), when 0.111 W is applied to each microheater region except the one to the right, resulting in a maximum temperature of 300 °C on the chip. **(c)**: Modelled temperature in the different regions when one (left) or three (right) of the regions are heated with a certain power.

(a)

(b)

(c)
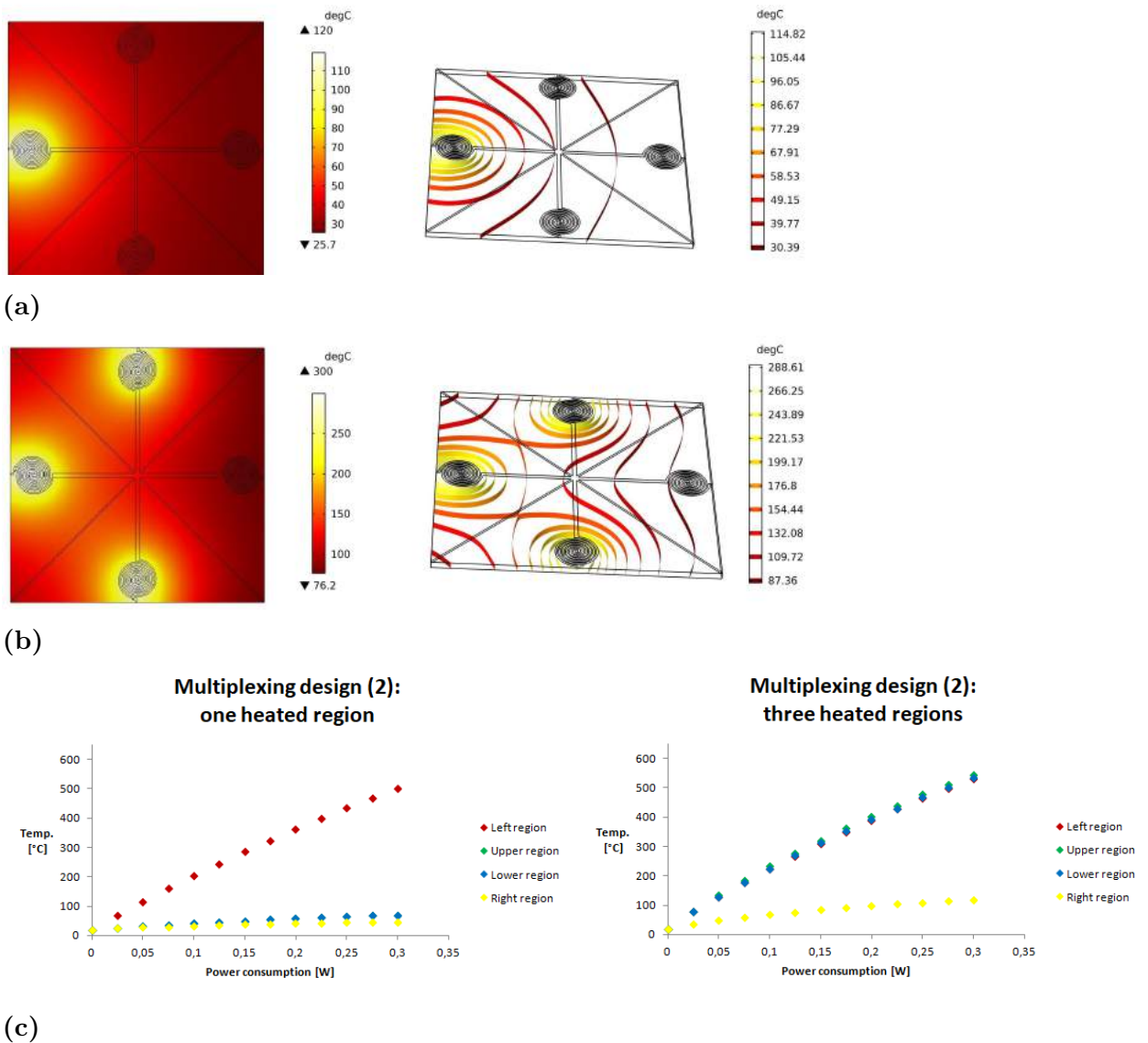
Figure 4.14: **(a)**: Temperature profile (left) and isothermal contours (right) for multiplexing design (2), when 0.051 W is applied to the left microheater region, resulting in a maximum temperature of 120 °C on the chip. **(b)**: Temperature profile (left) and isothermal contours (right) for multiplexing design (2), when 0.136 W is applied to each microheater region except the one to the right, resulting in a maximum temperature of 300 °C on the chip. **(c)**: Modelled temperature in the different regions when one (left) or three (right) of the regions are heated with a certain power.

(a)

(b)

(c)
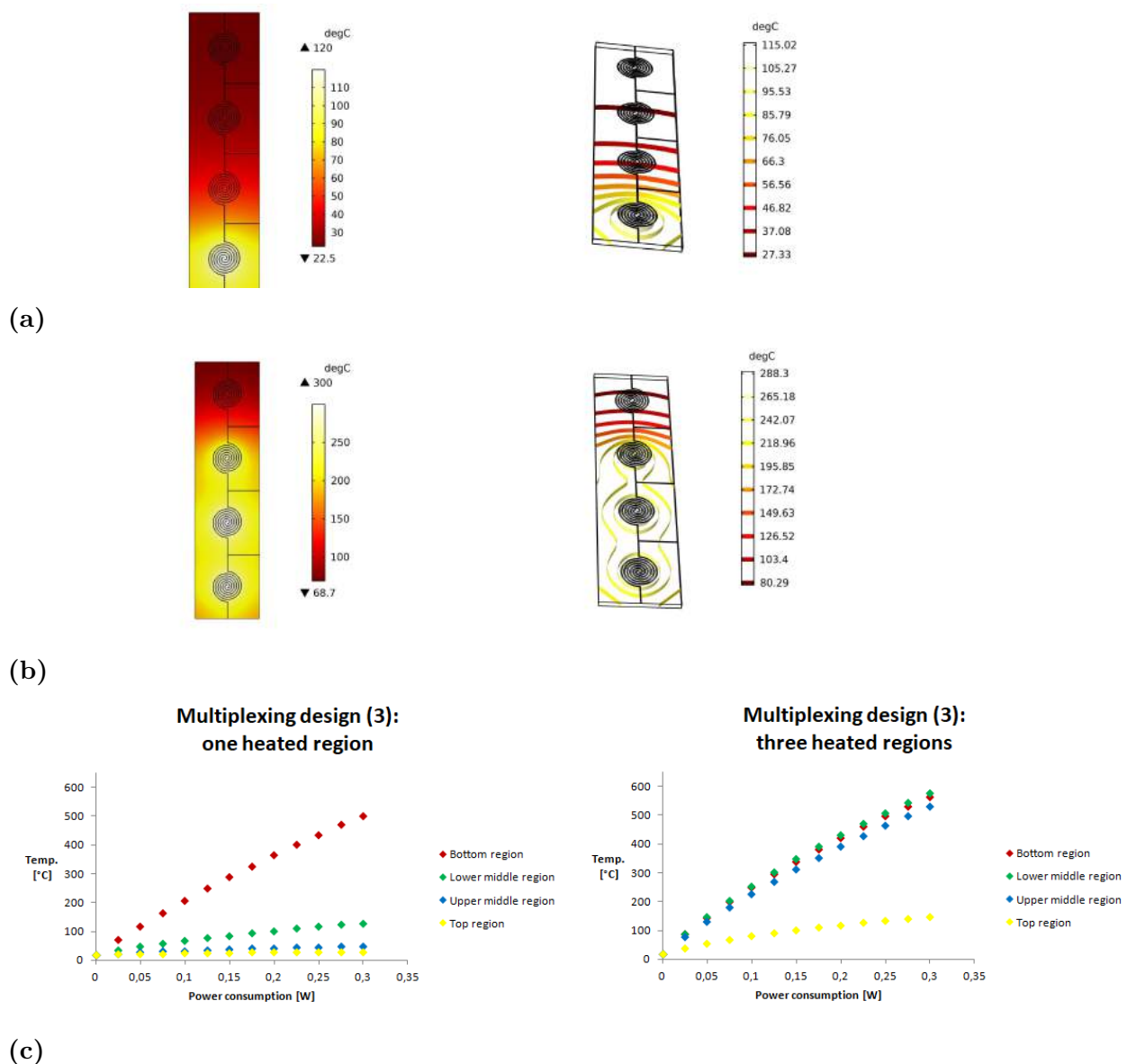
Figure 4.15: (a): Temperature profile (left) and isothermal contours (right) for multiplexing design (3), when 0.049 W is applied to the bottom microheater region, resulting in a maximum temperature of 120 °C on the chip. **(b)**: Temperature profile (left) and isothermal contours (right) for multiplexing design (3), when 0.123 W is applied to each microheater region except the one in the top, resulting in a maximum temperature of 300 °C on the chip. **(c)**: Modelled temperature in the different regions when one (left) or three (right) of the regions are heated with a certain power.

4.2.2 Fabricated multiplexing sensors

The three multiplexing designs that were modelled in section 4.2.1 have been fabricated and can be seen in figure 4.16, both when they are and are not wire bonded to the PCB:s. In table 4.6, the power consumption and voltage required to heat one

of the regions to 120 °C are stated, along with the electrical resistance. Moreover, in figure 4.17, measurements of power consumption and resulting temperature can be seen for the different multiplexing sensors, when one of the regions is heated. For multiplexing design (1)-(2), the estimated temperature in the other regions can also be seen. Calibration was not preformed for these sensors and instead an intermediate value of $0.0026\,K^{-1}$ was chosen as the TCR.

As stated in table 4.6, the power decrease compared to design (a) is 46-53 %, which is comparable to design (d). This is expected as the spiral regions in the multiplexing sensors are of roughly the same size as the one in design (d). However, according to the simulation results demonstrated in section 4.2.1, the required power to reach 120 °C should be 53-57 % lower than those measured. As the multiplexing sensors are wire bonded with thin electrodes, this error is likely not due to heat conduction to the electrodes which was a possible explanation for the modelling errors for designs (a)-(f). Rather, heat conduction to the PCB seems like a more plausible explanation.

The temperature distributions on the multiplexing sensors were also investigated with thermal imaging as seen in figure 4.18, where one of the regions are heated to approximately 120 °C. For multiplexing designs (1)-(2), the temperatures measured in the non-heated regions with the IR-camera seem to be in accordance with the thermoresistive measurements shown in figure 4.17. Additionally, the temperature profiles show similar behaviour as those predicted in section 4.2.1, even though the temperatures do differ slightly. Overall, when one of the regions is heated, it seems as if multiplexing design (2) has the lowest heat transfer to the remaining regions, while multiplexing design (1) has the highest. Multiplexing design (3) seem to be intermediate between the two other designs, but as displayed previously by the simulations, there is a relatively large temperature difference among the non-heated regions.

As previously mentioned, it does indeed seem like there is a prevalent heat conduction to the PCB, as a rather large area of plastic surrounding the heated region has an elevated temperature, according to figure 4.18. This could potentially be prevented or decreased by increasing the diameter of the holes below the sensing regions.

Furthermore, thermal images were taken of the multiplexing designs when two of the regions were heated by the same power, which can be seen in figure 4.19. As noticeable, the temperature of the remaining regions vary depending on where the two heated regions are positioned on the sensor. This is also true for the heated regions, since not both of them reach 120 °C. Generally it seems as if the two heated regions should be close to each other in order for the average temperature of the remaining regions to be minimal.
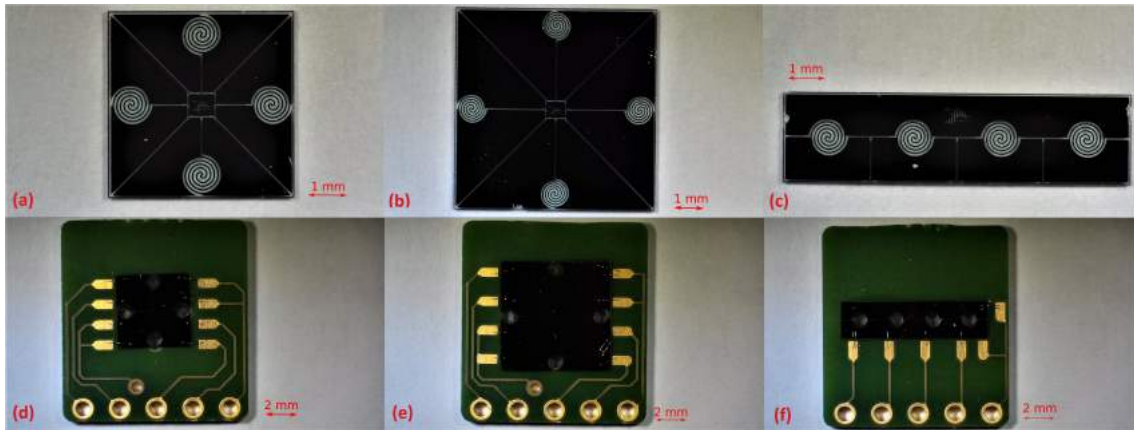
Figure 4.16: The different fabricated multiplexing sensors, both when they are and are not wire bonded to a PCB. **(a)**: Multiplexing design (1). **(b)**: Multiplexing design (2). **(c)**: Multiplexing design (3). **(d)**-**(f)**: The multiplexing sensors, when they are wire bonded to PCB:s.

Table 4.6: Tested properties of the three different multiplexing sensors. For all three sensors, the TCR has been assumed to be $0.0026\,K^{-1}$. For the modelled consumption change, the models displayed in section 4.2.1 are used.

Sensor	R(120 °C) [Ω]	U(120 °C) [V]	P(120 °C) [W]	Relative consumption change compared to design (a) [%]	Modelled consumption change [%]
Design (1)	182.60	4.36	0.104	-53	-66
Design (2)	189.89	4.72	0.118	-46	-65
Design (3)	187.08	4.56	0.111	-49	-66
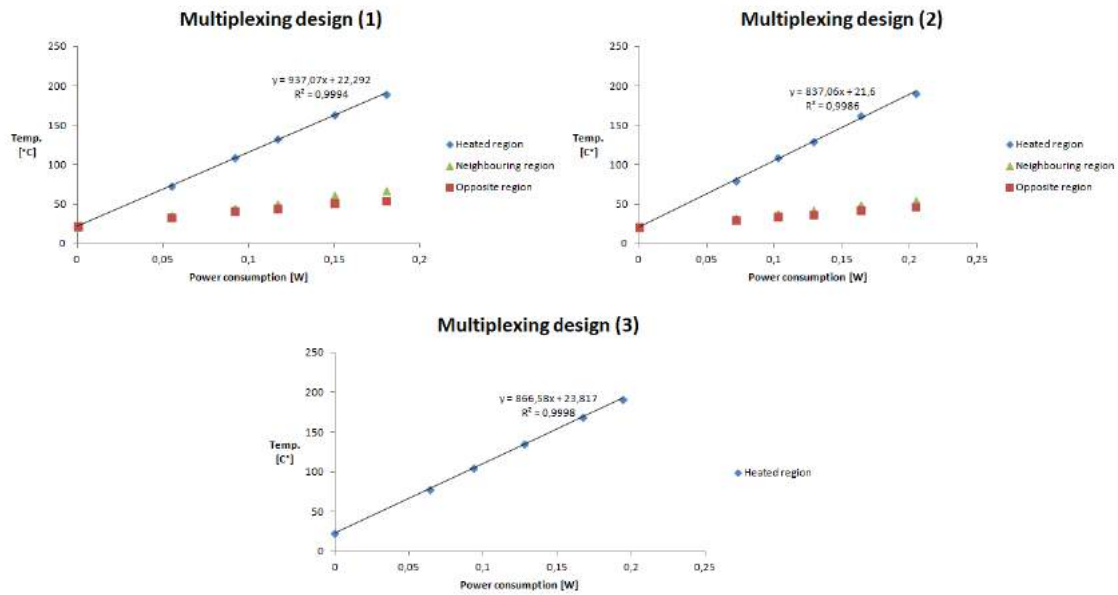
Figure 4.17: Graphs showing the relationship between power consumption and resulting temperature of the heated region, for multiplexing sensors (1)-(3). For multiplexing sensors (1) and (2), the temperatures of the other spiral regions are also shown. Neighbouring region refers to the two regions closest to the heated region, which are assumed to have approximately the same temperature due to symmetry, while opposite region refers to the region furthest away from the heated region. For multiplexing design (3), the temperature of the non-heated regions could not be determined, due to the contact layout on the PCB.
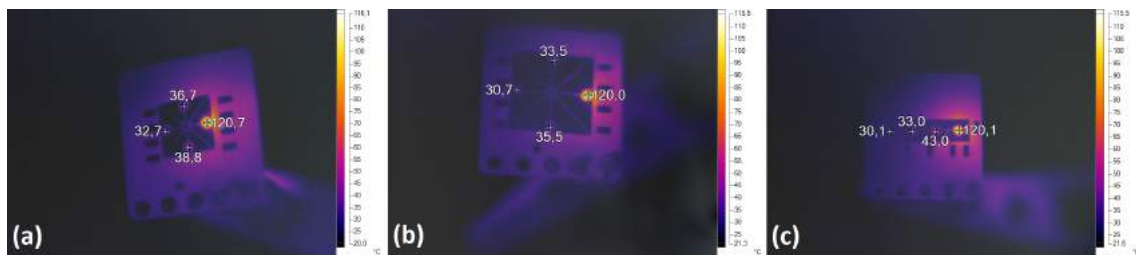
Figure 4.18: Thermal images of the multiplexing sensors, when one of the regions is heated to approximately 120 °C. The temperature scale is in °C.

42
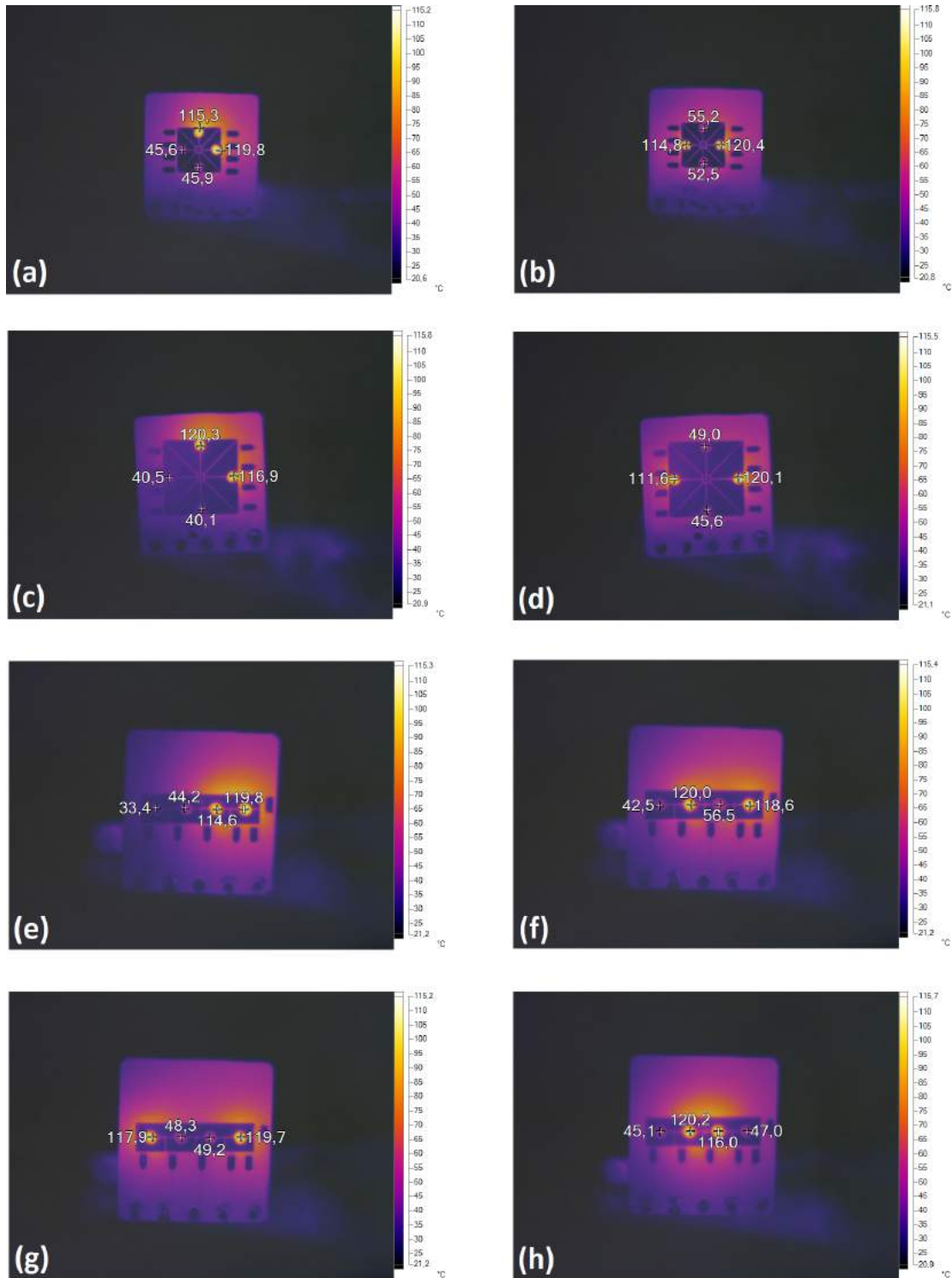
Figure 4.19: Thermal images of the multiplexing designs when the same power is applied to two of the regions, such that the maximum temperature of the sensor is approximately 120 °C. **(a)-(b)**: Multiplexing design 1. **(c)-(d)**: Multiplexing design 2. **(e)-(h)**: Multiplexing design 3.

5
Conclusions

In this project, several NPS sensors with micropatterned heaters have been modelled and fabricated for the purpose of yielding higher power efficiency and better thermal properties, both when utilised and not utilised for multiplexing. For decreasing the power consumption, the most promising alteration was to decrease the size of the active region utilised for sensing, in combination with decreasing the substrate thickness. This yielded a power decrease of approximately 51 % when compared to the currently used sensor design in *InAir*. Furthermore, by altering the microheater geometry it was possible to get a distinct decrease in electrical resistance, which could make it possible to power the heater with a low voltage battery and hence allow portable use. Through thermal imaging it was also established that a higher temperature uniformity of the heated region can be achieved by introducing either a groove or gap around the region, where the latter had the most prominent effect. Moreover, the IR-images also showed a relatively high temperature gradient towards the contact electrodes. This indicates that it might not be valid to neglect the heat transfer to the electrodes, which might explain why the modelled power consumption of the microheaters was lower than the actual.

Specifically for multiplexing, three different designs were modelled and fabricated, each with four different regions for the purpose of being able to maintain four different temperatures on the same sensor. Due to the multiplexing sensors having both a thin substrate and small size of the active regions, the power consumption to heat one of the regions was 46-53 % lower compared to the currently used sensor. For these fabricated multiplexing sensors, heating one of the regions to approximately 120 °C causes the other regions to reach temperatures of 30-43 °C, according to IR-images. Thermal imaging also revealed that there is a large heat transfer from the heated region to the PCB, which might explain why the actual power consumption of the multiplexing sensors greatly exceeded those predicted by the simulations.

5.1 Future work

The most pivotal aspect of the sensors is of course their sensing properties, hence a logical next step is to study how the NPS-analysis might differ among the fabricated sensors. For example, it should be properly investigated how sensitive the air quality measurement is to small temperature changes, in order to determine how important temperature uniformity is on the active region. As previously mentioned in section 2.3, temperature uniformity is important for signal quality in traditional

MEMS gas sensors. Since the plasmon peak is shifted with temperature in NPS, a low temperature uniformity should "smear" out the peak and hence decrease signal quality, but it remains to be studied exactly how strong this effect is for NPS gas sensing. As the plasmon peak's temperature dependence is strongly affected by the gas-SMO kinetics, the importance of temperature uniformity will also likely be somewhat different for different gases. Additionally, just as the temperature shift between the front- and backside of the sensors increased with increasing temperature, the temperature uniformity will likely be worse with increasing temperature, which might cause problems when sensing gases that require high temperatures. Furthermore, it should be investigated if the NPS properties are affected negatively when the size of the sensing regions is decreased, as this otherwise should be done to optimise the power consumption of the microheater.

For the sake of multiplexing, it is also of interest to establish exactly which temperatures that are required to sense different gases, as that will clarify whether the fabricated multiplexing sensors have good enough thermal properties to be able to individually maintain these temperatures.

Bibliography

[1] World health organisation (WHO). Ambient (outdoor) air quality and health [internet]. 2018 [cited 2019-02-15]. Available from: `https://www.who.int/en/news-room/fact-sheets/detail/ambient-(outdoor)-air-quality-and-health`.

[2] Svedendahl M.; Chen S.; Käll M. An introduction to plasmonic refractive index sensing. In Alexandre Dmitriev, editor, *Nanoplasmonic sensors.* New York, NY : Springer, c2012, 2012. pp. 1-22.

[3] Mayer K.M.; Hafner J.H. Localized surface plasmon resonance sensors. *Chemical Reviews*, (6):3828, 2011.

[4] Fredriksson H.; Alaverdyan Y.; Dmitriev A.; Langhammer C.; Sutherland D.S.; Zaech M.; et al. Hole-mask colloidal lithography. *ADVANCED MATERIALS*, 19(23):4297 − +, 2007.

[5] Larsson E.M.; Syrenova S.; Langhammer C. Nanoplasmonic sensing for nano-materials science. *Nano-photonics*, 1(3-4):249, 2012.

[6] Kasemo B. Zoric I. Langhammer C., Larsson E.M. Indirect nanoplasmonic sensing: Ultrasensitive experimental platform for nanomaterials science and optical nanocalorimetry. *NANO LETTERS*, (9):3529, 2010.

[7] M. Graf. *CMOS hotplate chemical microsensors. [electronic resource].* Microtechnology and MEMS. Berlin ; New York : Springer, c2007., 2007. pp. 1-3.

[8] Joy N.A.; Nandasiri M.I.; Rogers P.H.; Weilin J.; Varga T.; Kuchib-hatla S.V.N.T.; et al. Selective plasmonic gas sensing: H_2, NO_2, and CO spectral discrimination by a single $Au-CeO_2$ nanocomposite film. *Analytical Chemistry*, 84(11):5025–5034, 2012.

[9] Joy N.A.; Rogers P.H.; Nandasiri M.I.; Thevuthasan S.; Carpenter M.A. Plasmonic-based sensing using an array of Au-metal oxide thin films. *ANALYTICAL CHEMISTRY -WASHINGTON DC-*, (23):10437, 2012.

[10] Vuong N.M.; Kim D.; Kim H. Surface gas sensing kinetics of a WO_3 nanowire sensor: part 1—oxidizing gases. *Sensors Actuators: B. Chemical*, 220:932 − 941, 2015.

[11] Spruit R.G.; van Omme T.J.; Ghatkesar M.K.; Perez Garza H.H. A review

on development and optimization of microheaters for high-temperature in situ studies. *Journal of Microelectromechanical Systems*, (6):1165, 2017.

[12] Bhattacharyya P. Technological journey towards reliable microheater development for mems gas sensors: A review. *IEEE TRANSACTIONS ON DEVICE AND MATERIALS RELIABILITY*, (2):589, 2014.

[13] Simon I.; Barsan N.; Bauer M.; Weimar U. Micromachined metal oxide gas sensors: opportunities to improve sensor performance. *SENSORS AND AC-TUATORS B*, (1):1, 2001.

[14] Zhou Q.; Sussman A.; Chang J.; Dong J.; Zettl A.; Mickelson W. Fast response integrated mems microheaters for ultra low power gas detection. *Sensors Actuators: A. Physical*, 223:67 – 75, 2015.

[15] Welty J.R. *Fundamentals of momentum, heat and mass transfer.* Singapore : John Wiley Sons, cop. 2015., 2015.

[16] Karvinkoppa M.V.; Hotta T.K. Numerical investigation of natural and mixed convection heat transfer on optimal distribution of discrete heat sources mounted on a substrate. *IOP Conference Series: Materials Science Engineering*, 263(6):1, 2017.

[17] Jun gu K.; Joon-Shik P.; Kwang-Bum P.; Junho S.; Eung-An L.; Sangsoo N.; Hoo-Jeong L. Temperature control of micro heater using pt thin film temperature sensor embedded in micro gas sensor. *Micro and Nano Systems Letters, Vol 5, Iss 1, Pp 1-5 (2017)*, (1):1, 2017.

[18] Ida N. *Sensors, actuators, and their interfaces. [electronic resource] : a multidisciplinary introduction.* Edison, NJ : SciTech Publishing, [2014], 2014. pp. 67-80.

[19] Balboa I.; Silburn S.; Drewelow P.; Huber V.; Huber A.; Kinna D.; et al. Recent developments of in-vessel calibration of mid-ir cameras at jet. *REVIEW OF SCIENTIFIC INSTRUMENTS*, 87(11), 2016.

[20] Liu C.; Sui X.; Gu G.; Chen Q. Shutterless non-uniformity correction for the long-term stability of an uncooled long-wave infrared camera. *Measurement Science and Technology*, 29(2), 2018.

[21] Kittel C.; McEuen P. *Introduction to solid state physics.* Hoboken, N.J. : Wiley, c2005., 2005. pp. 148-151.

[22] Zhai Y.; Cai C.; Huang J.; Liu H.; Zhou S.; Liu W. Study on the resistance characteristic of Pt thin film. *Physics Procedia*, 32:772, 2012.

[23] Nordling C.; Österman J. *Physics handbook for science and engineering.* Studentlitteratur, 2006. pp. 44.

A

Appendix

A.1   Alternative heater geometries

Some alternative geometries, shown in figure A.1 have been modelled. When applying 0.145 W to each one these, the resulting temperature profiles are shown in figure A.2. A noticeable problem with designs (E), (F) and (J) (and to some degree design (K)) is that they suffer from highly localised heating centres in the connection points of the geometries, which could result in low mechanical stability in these structures. For design (A), (G) and (H), the heated area is more crescent than spherical in shape. This effect occurs due to these geometries being connected to the remaining metal film with several connection points. Since the source and ground are connected in the south edges of the film, more current will then travel in the lower part of the geometry to minimise the resistance, hence the crescent-shaped area of heating. This could be avoided by changing the arrangement of the electrode contacts such that they are more symmetrical in regards to the micropattern. For designs (I) and (K), due to the wire not covering a sufficient fraction of the sensor's active region, the temperature profile is not very uniform. Conclusively, designs (B)-(D) or (L) could potentially be an alternative to the circular double spiral. Though, as previously mentioned, rectangular shapes suffers from lower mechanical stability compared to circular ones. Design (L) is not a conventional design and hence not much is known about its properties in practice from previous studies.

A.2   Measurements on sensors with a single region

In figure A.3, the resistance change of the sensors can be seen as a function of temperature. According to equation 3.4, the TCR of the sensor is equal to the slope of the graph. In figure A.4, graphs showing the relationship between power consumption and microheater temperature can be seen for each sensor, where it can be seen that there is a good linear fit.
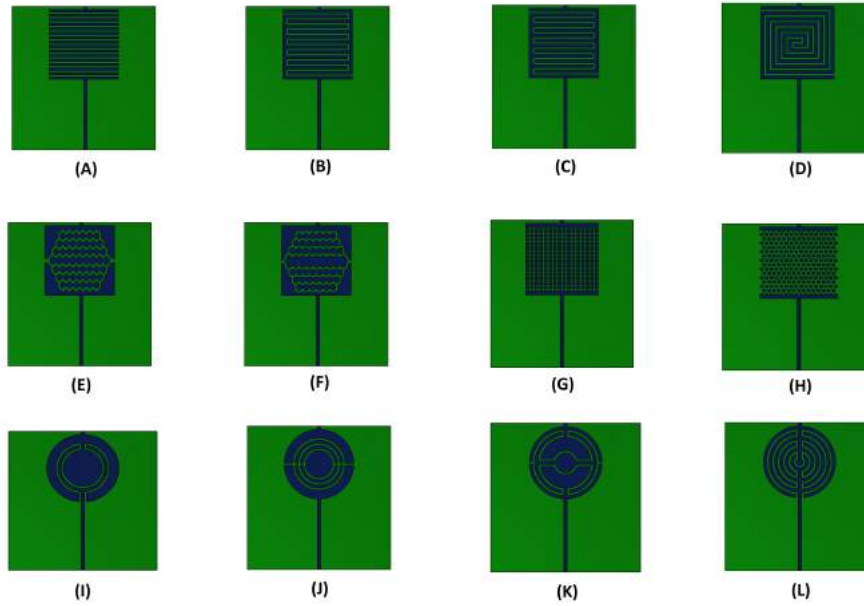
Figure A.1: Alternative heater geometries to the circular double spiral, that have been tested. (A) straight lines, (B) meander pattern, (C) meander pattern with curved corners, (D) rectangular double spiral, (E)-(F) jagged patterns with two connection points, (G) grid pattern, (H) sieve pattern, (I)-(L) different circular patterns.
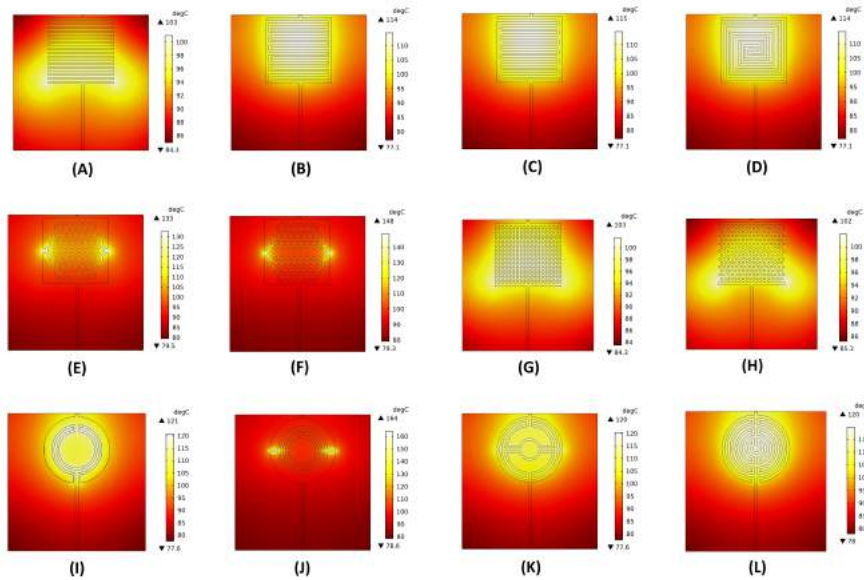
Figure A.2: Temperature profiles of the patterns shown in figure A.1, when 0.145 W is applied.
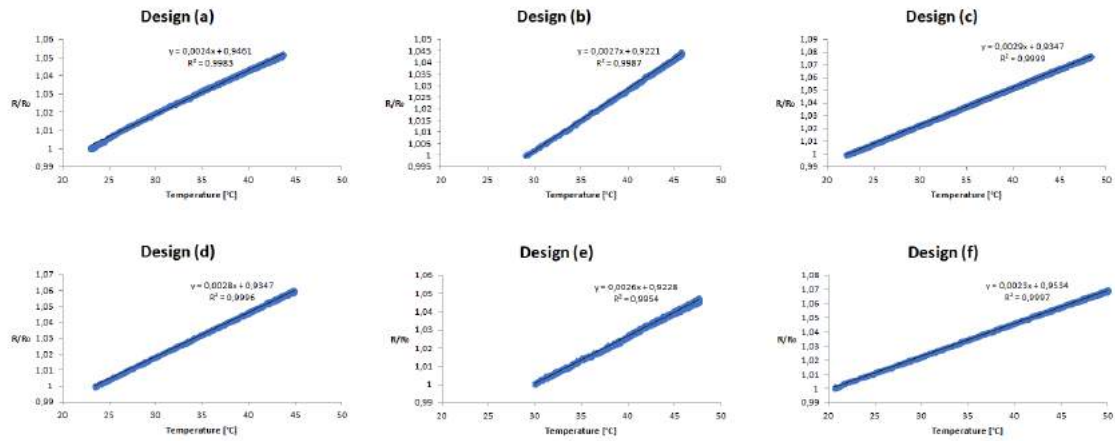
Figure A.3: Calibration curves for sensors (a)-(f), where the slope of the curve is the TCR for said sensor.
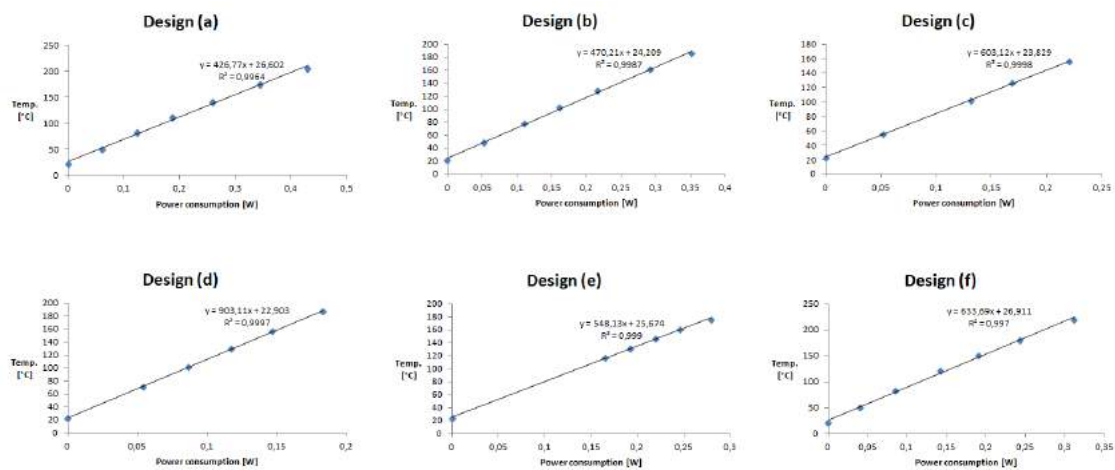
Figure A.4: Graphs showing the relationship between the power consumption and resulting temperature, for sensors (a)-(f).